The Pennsylvania State University
The Graduate School

LEAVES AND STEMS, ROTONS AND SOLITONS, MAGNETS AND ARRAYS, ONE GROUND STATE LOST, MANY FOUND, AND TWO FIELDS

A Thesis in
Physics
by
Cristiano Nisoli

Submitted in Partial Fulfillment
of the Requirements
for the Degree of

Doctor of Philosophy

May 2007

The thesis of Cristiano Nisoli was reviewed and approved* by the following:

Vincent H. Crespi
Professor of Physics
Professor of Materials Science and Engineering
Thesis Advisor, Chair of Committee

Peter C. Eklund
Professor of Physics
Professor of Materials Science and Engineering

Henry C. Foley
Professor of Chemical Engineering

Gerald D. Mahan
Distinguished Professor of Physics

Jayanth R. Banavar
Distinguished Professor of Physics
Department Head of Physics

*Signatures are on file in the Graduate School.

Abstract

A complete physical system typically requires three elements: particle, interaction, and manifold. Condensed matter physics provides a rich framework for generating new effective particles and new interactions such as quasiparticles, Cooper pairs or composite fermions. Rather than generate new effective particles or interactions within familiar flat space, one can also ask how novel geometrical constraints on the underlying manifold can generate new physics, even for old familiar interactions [1, 2].

Perhaps the simplest effective interaction is a featureless long-ranged repulsion, which leads to simple structures in flat space: in two dimensions, a triangular lattice. In contrast, interacting repulsive particles on a cylinder generate a rich degenerate family of helical structures that follow Fibonacci rules first seen in phyllotaxis, the study of plant morphology [3, 4, 5, 6, 7, 8]. After demonstrating phyllotactic patterns in an experimental "magnetic cactus" we show that linear dynamics of phyllotaxis generates rotons and the nonlinear regime supports a large family of dynamically stable topological solitons that can fragment, merge, or interconvert upon collision, with propagation speeds governed by energy conservation and phase matching. These new phenomena should be observable in a wide range of systems, from quantum to classical and from nanometer-scale to macroscopic.

In an attempt to mimic the zero point entropy of water and spin ice [9, 10, 11], we have engineered arrays of nanoislands, called "artificial spin ice" such that their simple magnetic interaction can be frustrated by their mutual disposition. While the magnetic cactus was degenerate - although not extensively so - yet could be annealed into its ground state, the artificial spin ice is theoretically non degenerate, yet attempts to anneal it yield a disordered state, described by an athermal manifold of extensive degeneracy. We show how to predict its non trivial thermodynamics with good agreement with experimental data and no fitted parameters,

using a principle of maximum likelihood reminiscent of entropy.

When a flat graphene sheet is rolled in the cylindrical geometry of a carbon nanotube, a mesoscopic system is born, with macroscopic length, yet atomic scale radius [12, 13, 14]. We will show here how to adapt to it the standard elastic formalism for macroscopic objects so that its atomic complexities can be taken into account, and yet still solved analytically. Disparate experimental and numerical results find explanation in this unifying framework.

Disclaimer: this is a steroid-free thesis: it was not "bulked up" with anabolic injections of previously know methods or of accepted theories, which could be found in countless variations of flavors in reviews, textbooks, and other thesis. To the best of our knowledge, it reports only novel results, how interesting or relevant being left to the reader to decide. Attempt was made to write it in a self consistent way, to a level accessible to a graduate student in physics. We have added only a small introduction to elasticity of continua in Chapter 2, since it seems more common of curricula in engineering rather than in physics, in USA.

Table of Contents

List of Figures

List of Tables

Acknowledgments

Prof. Vincent (Vin) H. Crespi, my advisor, allowed me to pursue diverse ideas with different methods while at the same time helping me land on charted territories. His liberality toward my inclinations made my graduate experience a happy one, and must be credited with (blamed for ?) the variety of subjects and scopes this thesis contains. It is well known that Vin is a volcano of ideas, knowledgeable in almost everything in (and out of) condensed matter physics. He is also a good buddy for an evening with sangria and tapas.

As enjoyable as useful, discussions with Dr. Paul E. Lammert have helped me overcome obstacles, formalize ideas, find inspiration and sharpen mathematical rigor. Of course Paul is not a human being. It is said that on the planet he comes from, people have been genetically engineered to be caring and selfless, theoretical physics is taught in Kindergarten, and toddlers are being read Borges and Dante at bedtime – those few who cannot read since birth.

Scientific research is a cooperative endeavor.

Nathan Gabor, then in Prof. Maynard's group, currently at Cornell University, performed the experiment described in Chapter 1, Section 2.

I had useful discussions with Prof. Eric Mockensturm: among other things he found out that my many-field idea had actually already been introduced by R. D. Mindlin of Columbia University, some 35 years before.

RuiFang Wang, with Prof. Schiffer's group and collaborators, performed the experiment on Artificial Spin Ice, with commendable hard work.

I extend my thanks to all these scientists and to all the wonderful, hardworking, passionate people of the Physics Department at Penn State.

I also thank my parents, who provided me with an education, yet never actually complained that I never found a real job – much to my surprise.

And my wife, Donatella, who thinks I am much better than what I really am, and thus makes me better than I would have been.

And my daughters, Beatrice, Victoria and Christina; they are the best thing past, present or future.

Dedication

On the front page of his discharge papers, section "Decorations and Merits", I can read the date "december, 15, 1941, XX of the fascist era". Of the location only I can only understand "russian front".

Twenty-four year old Sergente Maggiore Tarcisio Iseni, was running in the snow, after a sled, in a mission to transport certain supplies. Just a few instants before the facts – as he told me years later – he had reached for the driver: "Jump out, it's your time to run". "You can run a little more Sir, I'm not quite frozen yet". Tarcisio went back running, then the blast. He emerged shocked from a pit in the snow where the explosion had thrown him; the sled was smoking, the horse that had stepped on the land-mine disintegrated, the other one still standing, its organs dropping from the open belly, the driver half naked, gravely wounded, unconscious but still alive.

Tarcisio did everything he could to save him: he "covered him with his own clothes to protect him from the intense cold", as the elegant handwriting that motivates the Encomio Solenne reports. He "carried him for a long way", out of the mined field. He succeeded and delivered him still alive to medical care "a beautiful example of altruism and sense of duty toward a dependent". All in vain of course, the soldier died soon after.

A gesture of friendship switched fates, condemned its author, saved the life of my maternal grandfather. Because of that I am here now, and quite a few other people with me. That is of course only one of the uncountable, completely fortuitous events that call us into existence, yet it is one I know of. And thus I dedicate this thesis to that anonymous soldier and to my grandfather Tarcisio.

Chapter 1

Stems, Leaves, Rotons and Solitons, Ground State Found

"I perhaps owe having become a painter to flowers. "

Claude Monet

Symmetrical morphologies and regular patterns in living organism have been credited with originating the idea of beauty, the notion of art as imitation of nature, and with having first motivated humans toward mathematical inquiries [15]. The fascinating symmetrical patterns (Figure 1.1) of organs in plants studied by Phyllotaxis [7, 3, 4, 5] were known to Romans (Pliny) and ancient Greeks (Theofrastus), while early recognitions are found in sources as ancient as the Text of the Pyramids [7]. Leonardo da Vinci [16], Andrea Cesalpino and Charles Bonnet [17] explored phyllotaxis in the modern era. Kepler proposed to use the Fibonacci series 1, 2, 3, 5, 8..., in which each term after the second is the sum of the two preceding ones [18], to describe the phyllotactic patterns.

A discipline that thrived on multidisciplinary interactions [19], phyllotaxis found its standard mathematical description when August and Louis Bravais [20] introduced the point lattice on a cylinder to represent leaf distribution on a stem. In the simplest case (Figure 1.2), the phyllotactic lattice consist of a generative spiral of divergence angle Ω, on which the parastichies (oppositely winding "visible" spirals of plants) joins elements to their nearest neighbors. The numbers (n, m)

Figure 1.1. Phyllotaxis in a *Mammilaria Gigantea*.

of crossing parastichies represent consecutive terms of the Fibonacci series – or of the two generalizations obtained by varying the two initial terms: 1, 3, 4, 7, 11..., and 1, 4, 5, 9..., called second and third Phyllotaxis; consequently, the divergence angle assumes in botanical species values close to [21, 4]

$$\Omega_p = \frac{360^o}{(\tau + p)}, \tag{1.1}$$

where $p = 1, 2, 3$ labels the phyllotaxis kind, and

$$\tau = \left(1 + \sqrt{5}\right)/2, \tag{1.2}$$

is the Golden Ratio. For more than one generative spiral (multi-jugated phillotaxis), parastichies share a common divisor $(n, m) = (kn', km')$, k the number of generative spirals [21, 4]. Not unlike crystals, plants show kinks between domains, called transitions by botanists [22].

Unfortunately botanists neglected the work of the Bravais brothers, and it wasn't until Church rediscovered it eighty years later that more progress was done in the field [6]. In the last 50 years, phyllotactic patterns have been seen or

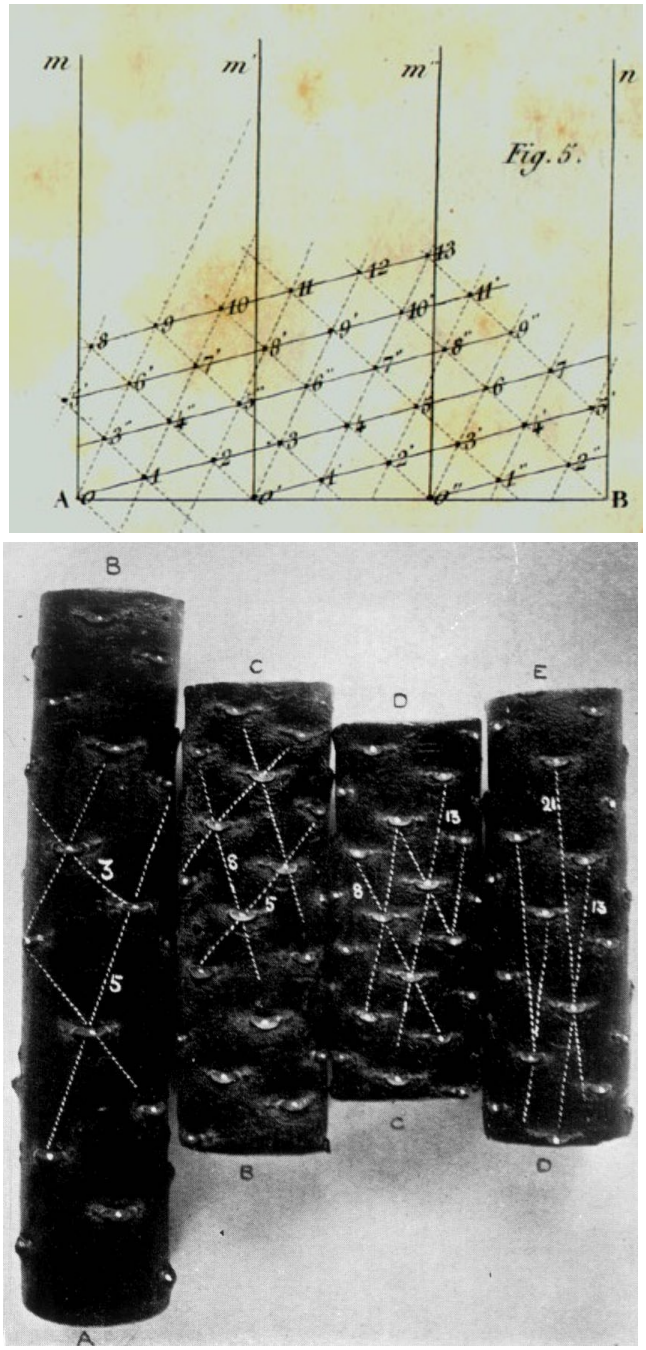

Figure 1.2. Top: the lattice from the seminal Bravais (1837) publication [20]: points are numbered along the generative spiral, parastichies connect nearest neighbors. Bottom: *Euphorbia Wulfenii*. Stem 15 mm in diameter. Various systems of parastichies on a continuum portion of the axis A, B, C, D, E, from the original publication (1904) of Church [6]

predicted outside the domain of botany as well: in the structure of polypeptide chains [23, 24], in tubular packing of spheres [25], self-organized growth [26], in layered superconductors [8], fluid dynamics [27], and more recently in self assembled microstructures [28].

Recently an energetic approach to phyllotaxis was proposed by Levitov, who predicted phyllotactic patterns for vortices in layered superconductors. Levitov's energetic approach returns phyllotactic patterns as configurations of minimal energy of a cylindrical lattice of repelling objects, the repulsion mimicking the rigidity of the plants units. Yet, such constraint to a lattice is absent both in botany and in the many physical systems contemplating repulsive particles in cylindrical geometries, from flux lattices [8] to cooled particle beams [29, 32, 30, 31], to adatoms or low density electrons on carbon or boron nitride nanotubes.

1.1 Annealing into Phyllotaxis.

1.1.1 Energetic Approach to Phyllotaxis

In a groundbreaking work, Levitov showed that a cylindrical lattice of repulsive particles is described by Phyllotaxis [8, 33, 34]. Levitov's underlying hypothesis, that phyllotactic ground states are 2-D Bravais lattices, has never been proved. We have verified that hypothesis experimentally by means of a "Magnetic Cactus" of magnets (spines) mounted on stacked co-axial bearings (stem) with south poles all pointing outward. When annealed, our "magnetic cactus" precisely reproduces botanical phyllotaxis. We thereby demonstrate for the first time that phyllotaxis is a ground state. Unlike biology, a mechanical phyllotactic system has dynamics; we will show in another section that this includes not just annealing but also rotons and solitons. In addition to our macro-scale implementation, such systems could also be created at the quantum level in nanotubes or cold atomic gases.

1.1.2 A Magnetic Cactus

To prove experimentally that 2-D point lattices are phyllotactic ground states in an unconstrained system, we construct a "magnetic cactus" consisting of 50 permanent magnets (spines) mounted on stacked co-axial bearings (stem), Figure 1.3,

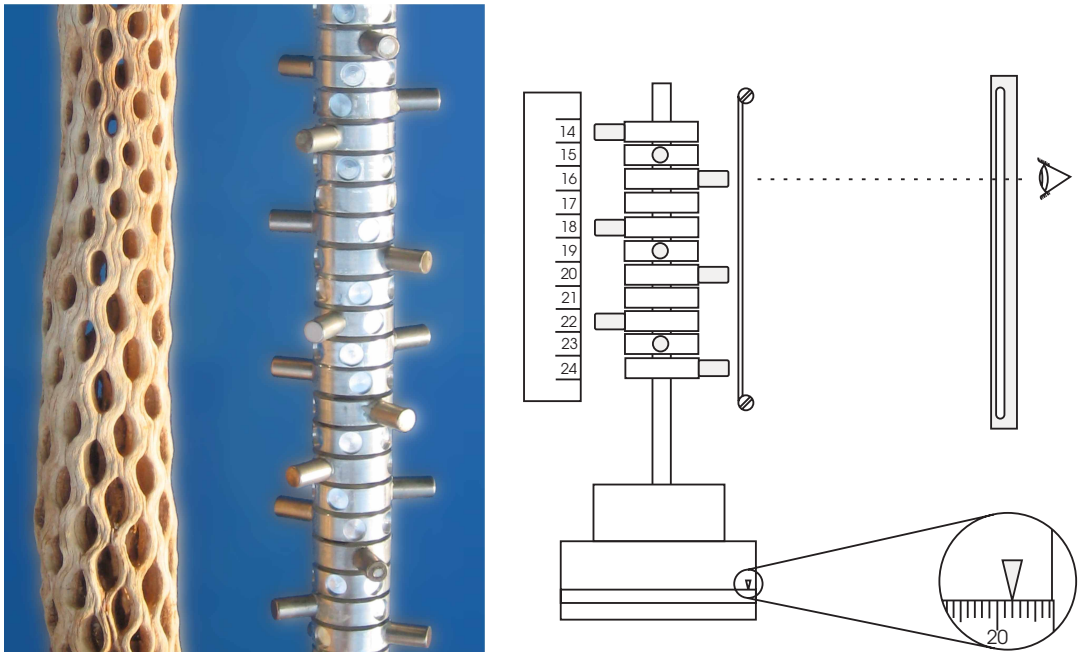

Figure 1.3. Left: Mammilaria elongata (golden star cactus) and the magnetic cactus. Right: Technical description of the experimental apparatus.

with south poles all pointing outward to produce a repulsive interaction between magnet pairs, and free to rotate about the central axis. The apparatus rests in the vertical position, centered by the supporting structure, Fig 1.3; Two versions of the same apparatus were used; the second, with magnets twice as long as the first. Previous successful attempts to reproduce phyllotactic patterns in experimental apparati include the optimal packing of metal spheres by Airy [35], and the droplets of ferro-fluid in a magnetic field in the recent, fundamental work by Douady and Couder [26]. Nathan Gabor, then an undergraduate in Prof. Maynard's group, built the magnetic cactus and performed the experiment.

Before every data acquisition, the cactus is disordered: the system is winded until the magnetic element structure undergoes an explosive release of energy and the magnets settle into a disordered configuration; then possible long range patterns are further disrupted by oscillating an independent hand-held magnet in small circular motion near some randomly chosen point while the cylinder is again rotated slowly. Finally, a random number of magnetic elements are interchanged between adjacent unit rings, an action which *clicks* one magnet into the spot formerly occupied by a neighboring magnet. Then the magnetic cactus is annealed

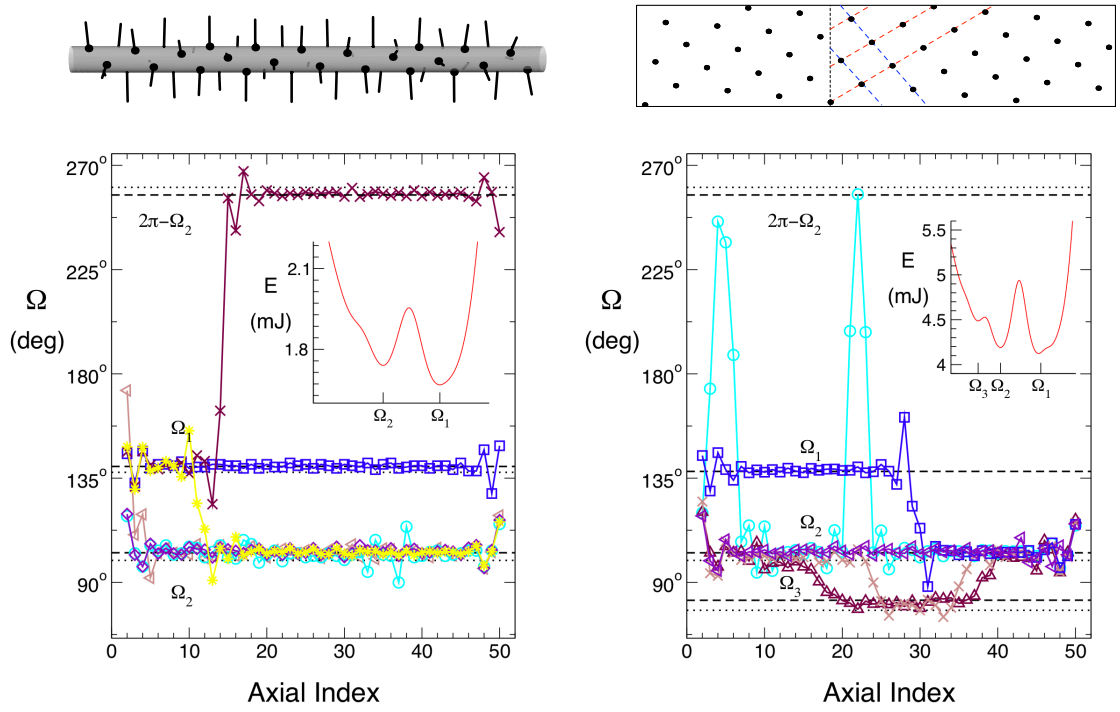

Figure 1.4. Results of Annealing: A 3-D rendering (top left) and the corresponding Bravais lattice (top right) of the magnetic cactus annealed in a spiraling configuration of divergence angle Ω_1 and parastichies (2,3) (blue and red dashed lines). Ω, the measured divergence angle between consecutive magnets, *vs.* axial index for the arrangement with one magnet (bottom left) and two magnets stacked on top of each other (bottom right). Dotted lines correspond to angles Ω_1, Ω_2, Ω_3, $2\pi - \Omega_2$, dashed lines to the minima of the magnetic energy in the spiraling ensemble. Insets: the curves for the energy per magnet (calculated after interpolating measured values for the pair-wise magnet-magnet interaction as a function of distance and orientation) of the spiralling pattern as a function of the divergence angle.

via random oscillations of rotation and vibrations for 10–30 seconds: this is accomplished manually, buy unlocking the stem at the top, and flipping it back and forth while shaking it, at the same time.

For the first magnetic cactus we find that the magnets self organize into spirals, their divergence angles precisely reproducing angles of first ($\Omega = \Omega_1$, parastichies $(2, 3)$) and second phyllotaxis ($\Omega = \Omega_2$, parastichies $(3, 4)$) of Equation (1.1), Figure 1.4. In the cactus with longer magnets, third phyllotaxis domains are observed as well ($\Omega = \Omega_3$, parastichies $(1, 4)$), bracketed by second phyllotaxis domains. In Figure 1.4 we report results for both cases, along with the energy per magnet (calculated after interpolating measured values for the pair-wise magnet-

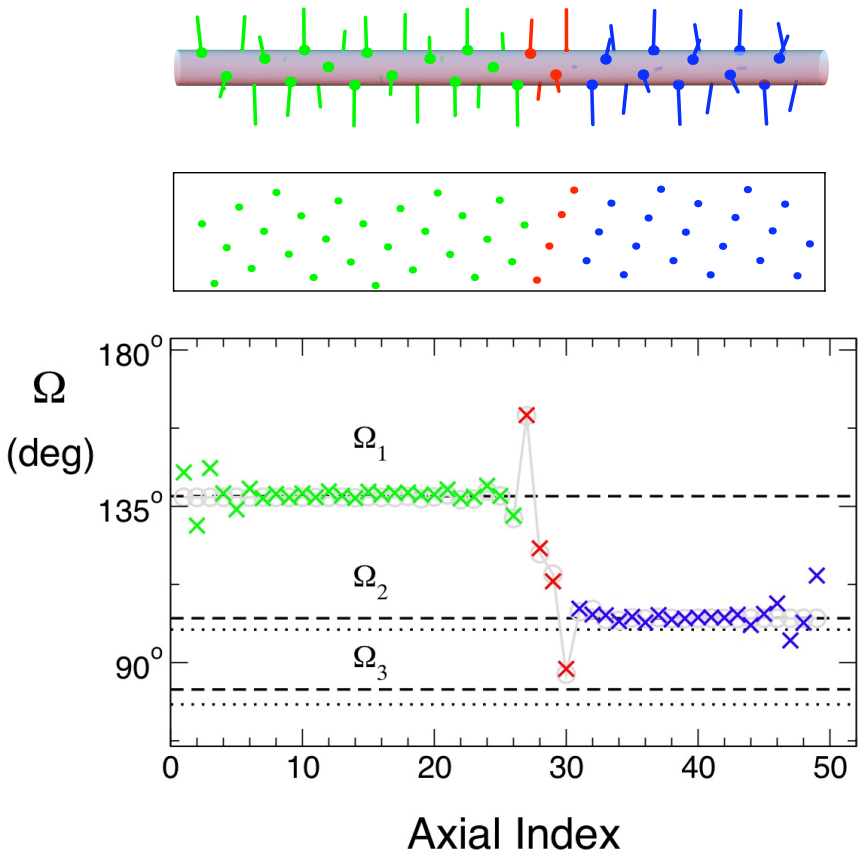

Figure 1.5. Top: 3-D rendering of a kink between domains of first and second phyllotaxis (b.) its 2-D Bravais lattice. Bottom: measured (Xs) and numerically calculated (Circles) divergence angles between consecutive magnets, *vs.* the axial index.

magnet interaction as a function of distance and orientation) of the spiralling pattern as a function of the divergence angle.

In many instances we observe a fragmentation of the system in two or three different domains, always sharing a common parastichy, separated by a domain wall, as seen in botany [22]. We have computed numerically one such transition via dynamical simulation. The interaction used in the simulation was calculated after interpolating measured values for the pair-wise magnet-magnet interaction as a function of distance and orientation, in order to reproduce the experimental apparatus behavior. A static step-like kink, imposed as an initial condition, radiates energy in the form of traveling waves; when the resulting configuration is

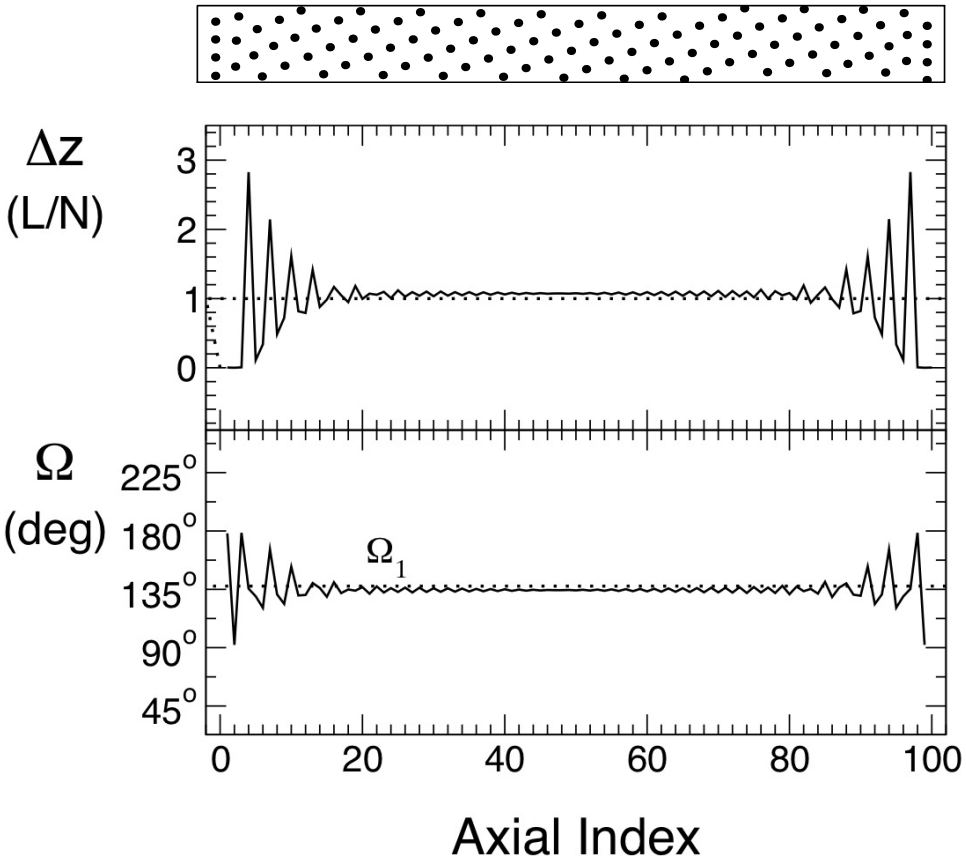

Figure 1.6. Top: Numerical Optimization via Structural Genetic Algorithm for $N = 101$ repulsive particles ($V = V_o(r_o/r)^2$) constrained on a cylindrical surface of length L and radius $R = 1.65L/N$ returns a 2-D Bravais lattice. Bottom: $\Delta z = z_{i+1} - z_i$, the difference in axial coordinate between consecutive particles and Ω, the angular divergences between consecutive particles, *vs.* the axial index: besides fringe effects at the border of the potential well, in the bulk particles align themselves on a single spiral of divergence $\Omega = \Omega_1$, from Equation 1.1. For larger values of NR/L whorled phyllotaxis (corresponding to more than one spiral) can be found.

temporally averaged to remove residual oscillations and then used as new initial conditions, the resulting kink is static, and matches perfectly the experimental data, as reported in Figure 1.5.

1.1.3 A Structural Genetic Algorithm

The magnetic cactus is only partially unconstrained: magnets in it cannot move axially. To study the case where repulsive object can move axially as well as

angularly on the the cylindrical surface, we employed a non local numerical optimization of the energy of the *completely* unconstrained system via a Structural Genetic Algorithm.

While traditional genetic algorithms had but a few successful applications to the physical sciences, the Structural Genetic Algorithm introduced by Deaven and Ho [36] does not work with an artificial genetic sequence, but directly with the structure itself and allows physical intuition in tailoring a suitable mating scheme that accelerates convergence. It has proved itself very efficient [37] in tackling the Thomson problem of repulsive charges on a sphere [1] and even in finding fullerene structures [36].

Our mating procedure chooses mates randomly, cuts the parent lattices at a random axial coordinate and then swaps top and bottom. We run our structural genetic algorithm for a system of $N = 101$ repulsive particles, interacting via $V = V_o(r_o/r)^2$, constrained by a potential well in the axial coordinate $(0, L)$ using 10 parents and 10 children at every generations. To avoid population bottlenecks, we change the 3 higher energy members of the populations anyway: those of them that cannot be replaced by children will be mutated in various ways, which typically leads to structures of much higher energy.

After typically 15-20 generations, our Genetic Algorithm returns a two-dimensional cylindrical crystal, as expected. Even for large radii, where configurations corresponding to more than one generative spiral (multi-jugated phylltaxis) would enter in the ground state degeneracy, the genetic algorithm returns simple phyllotaxis with degenerative angle Ω_1.

In Figure 1.6 we report results for radius $R = 1.65L/N$, $N = 101$. The Structural Genetic Algorithm returns a single spiral of divergence Ω_1, from Equation 1.1, corresponding to first Phyllotaxis with parastichies $(1, 2)$. The plot of $\Delta z = z_{i+1} - z_i$ returns the value L/N in the bulk, which points to a single generative spiral.

Early populations provide metastable very disordered states; intermediate ones show kinks among domains of opposite divergence angle.

In conclusion we have demonstrated experimentally and numerically for the first time that 2-D point lattices of proper angles are phyllotactic ground states in an unconstrained system, a fact relevant not only for botanical phyllotaxis, but

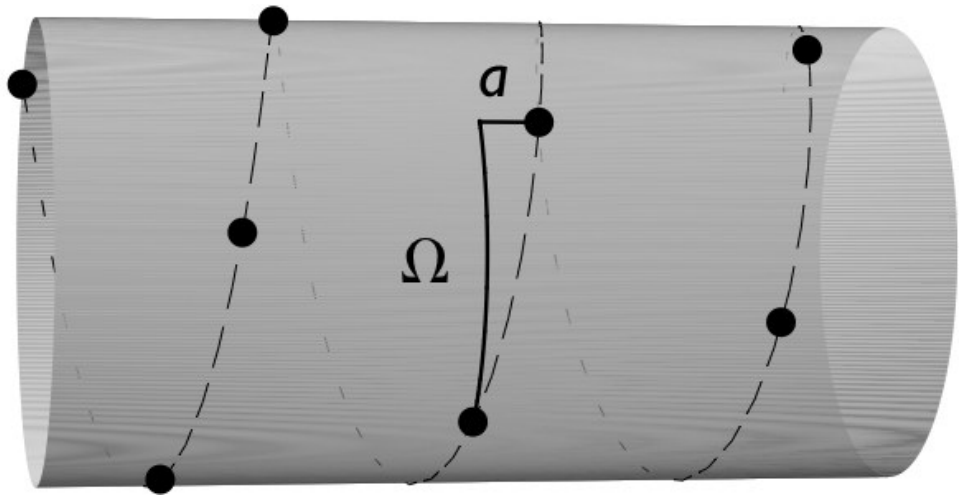

Figure 1.7. Repulsive particles arrayed along a one-dimensional Bravais lattice wrapped onto the surface of a cylinder. a is the axial separation between particles and Ω is the screw angle.

for many physical systems of repulsive particles in cylindrical geometries.

As we anticipated such systems can access various degrees of dynamics, providing new phenomenology beyond botany. We are going to explore that in the next section.

1.2 Dynamical Phyllotaxis

1.2.1 Phyllotaxis in Physical Systems

Classic botanical phyllotactic systems such as cacti do not possess dynamics (aside from slow growth), but many alternative physical realizations of phyllotactic systems previously mentioned can show dynamical phenomena. Here we demonstrate that the linear dynamics of phyllotaxis generates rotons and the nonlinear regime supports a large family of dynamically stable topological solitons that can fragment, merge, or interconvert upon collision, with propagation speeds governed by energy conservation and phase matching.

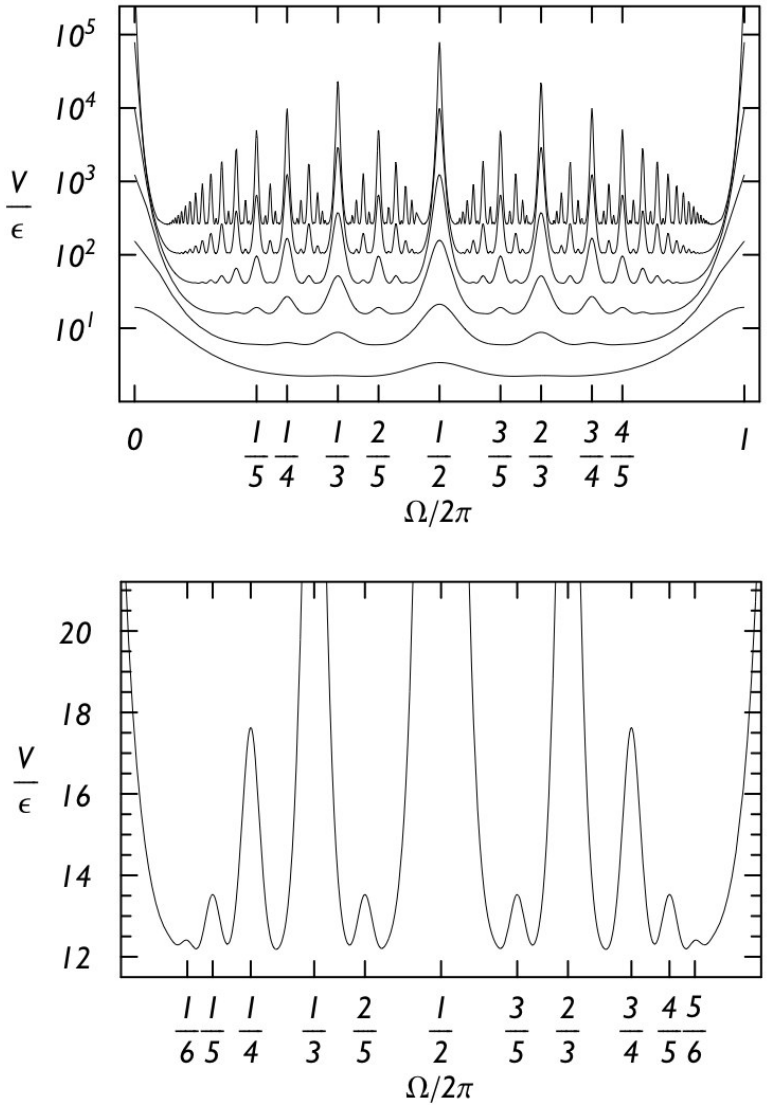

Figure 1.8. Lattice energy $V(\Omega)$ versus screw angle for successively halving values of a/R starting from 0.5 (top), and in detail for $a/R = 0.15$ (bottom). The highest rank observed, $J = 6$, matches Equation 1.7.

1.2.2 Degeneracy

To describe phyllotaxis, we assume a Bravais lattice structure in one dimension, wrapped helically (with an axial spacing a) onto a cylinder of radius R, as shown in Figure 2.2. At a given density this lattice is described by a single parameter Ω, the screw angle between successive particles. For a generic pair-wise repulsive

interaction v_{ij} between particles i and j, the energy of the static lattice is

$$V = \frac{1}{2}\sum_{i\neq j} v_{i,j}. \tag{1.3}$$

Since the lattice structure is defined by Ω, we can write $V(\Omega)$. The lowest-energy spiral at low density (i.e. large a/R) has $\Omega = \pi$, since that angle generates the largest inter-particle separation. At a slightly higher density, the second neighbor according to the Bravais lattice becomes the first neighbor in real space, and the angle π becomes unfavorable. As a/R decreases, the number of maxima in $V(\Omega)$, increases. For a/R low enough, any commensurate spiral of screw angle

$$\Omega_j^i = \frac{2\pi i}{j} \tag{1.4}$$

with i, j relatively prime becomes a local maximum, called a peak of *rank* j, as in Fig 1.8.

The degeneracy of $V(\Omega)$ will be important to the dynamics of solitons, so we develop it here. Peaks of equal rank are nearly degenerate, since their principal defining energetic contribution arises from particles facing each other at a distance ja. The minima also become more nearly degenerate as the density increases, since for angles incommensurate to π each particle is embedded in a nearly uniform background charge from the other particles. We can relate the degeneracies of both minima and maxima to purely geometrical parameters. Grouping peaks into families of equal rank

$$P_j \equiv \{\Omega = 2\pi i/j \mid \text{for } i,\, j \text{ coprime and } i \leq j\} \tag{1.5}$$

generates a Farey class of order j [40], i.e. all fractions in lowest terms between 0 and 1 whose denominators do not exceed j. The cardinality of P_j is Euler's totient function, $\phi(j)$. The degeneracy D of the energy minima for a system with a maximum peak rank J is then [41, 42]

$$D = \sum_{j=1}^{J} \phi(j) = \frac{3}{\pi^2} J^2 + O\left(J \log J\right), \tag{1.6}$$

which scales as $D \sim 2R/a$: new peaks of rank J appear at $\Omega = 2\pi i/J$ (i, J coprime) when the distance (in three-dimensional space) between particles separated axially by a equals that between particles separated axially by Ja. For reasonably large values of J,

$$J = \left[\left[\sqrt{\frac{2\pi R}{a}}\right]\right], \tag{1.7}$$

where $[\![\ ]\!]$ denotes the integer part. A minimum in $V(\Omega)$ bracketed by peaks of rank j_1 and j_2 corresponds to a rhombic lattice where each particle has its nearest neighbors at axial displacements of $\pm aj_1$, $\pm aj_2$ and second nearest neighbors at $\pm a(j_1 + j_2)$ or $\pm a(j_1 - j_2)$ [8]. The so-called parastichy numbers j_1 and j_2 give the number of crossing secondary spirals (parastichies) needed to cover the lattice by connecting nearest neighbors.

1.2.3 Phonons and Rotons

To study dynamics, we constrain the particles to fixed axial positions ia, leaving the angular coordinates θ_i as dynamical variables. The resulting excitations are similar to the transverse modes of an axially unconstrained system. The total energy is

$$E = \frac{1}{2} I \sum_i \dot{\theta}_i{}^2 + V. \tag{1.8}$$

For specificity, we take the particles as dipoles $\boldsymbol{p}$ directed radially outward [1], but the essential results apply to any reasonably smooth and long-ranged potential. The natural energy and frequency scales are $\epsilon = p^2 R^{-3}$ and $\tau = \epsilon^{-1/2} I^{1/2}$.

Consider oscillations

$$\theta_n = \bar{\Omega}\, n + \psi_n(t), \tag{1.9}$$

around a stable structure $\bar{\Omega}$, with normal modes

$$\psi_n(t) = \Psi_k \cos\left[kn - \omega(k)t\right]. \tag{1.10}$$

The most important interactions are between nearest neighbors in space, which generally are *not* nearest neighbors on the underlying one-dimensional geometry.

[1] Their interaction is repulsive at the densities studied.

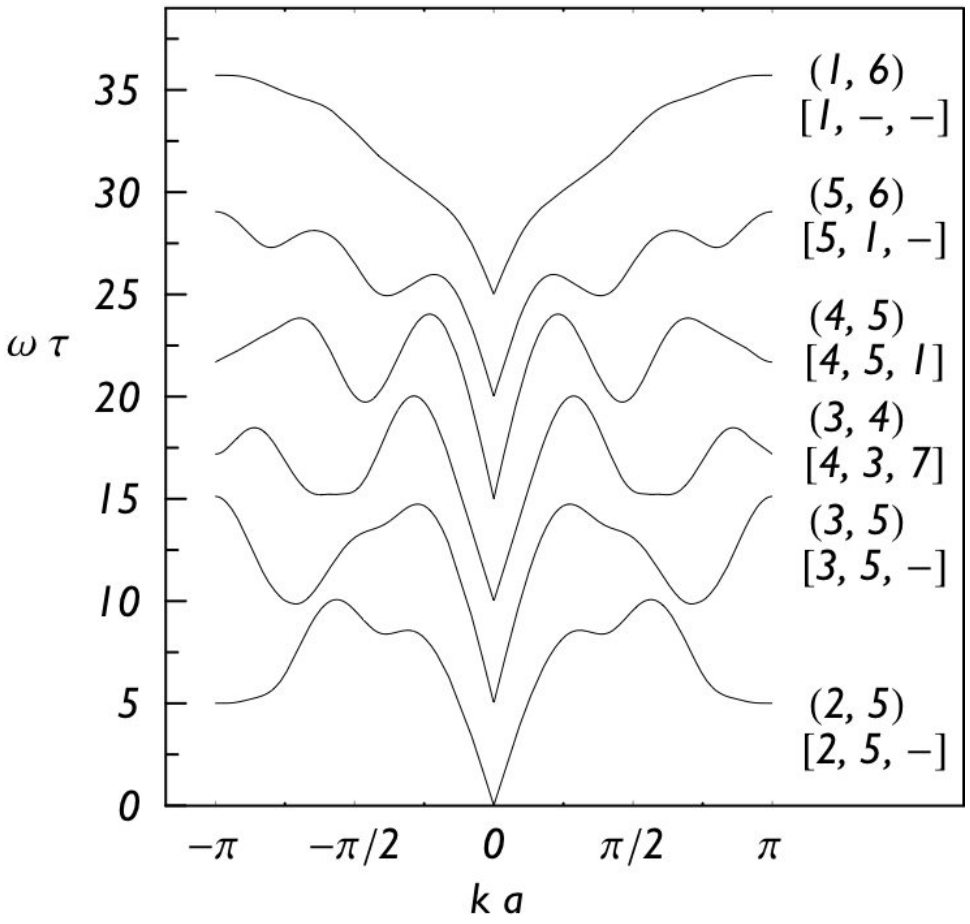

Figure 1.9. Phonon dispersion relations for the structures in the lower panel of Figure 1.8, each spectrum offset by 5 T^{-1} for clarity. Corresponding parastichy numbers $(j_1,\ j_2)$ and nearest three neighbors $[\tilde{j}_1,\ \tilde{j}_2,\ \tilde{j}_3]$ with $(\omega_1\tilde{j}_1 > \omega_2\tilde{j}_2 > \omega_3\tilde{j}_3)$ are given. The simple estimate for the number of rotons and maxons, $2\tilde{j}_1 - 1$, holds for all but (2,5).

Thus, we express the frequency as

$$\omega(k)^2 = 2\omega_{j_1}^2[1 - \cos(j_1 k)] + 2\omega_{j_2}^2[1 - \cos(j_2 k)] + \cdots \tag{1.11}$$

where j_m is the relative index of the m-th neighbor (*e.g.,* $j_1 = 4$ for the $(4, 5)$ structure) and ω_m is proportional to the second derivative of $v_{0,m}$ at the equilibrium positions defined by $\bar{\Omega}$. The wave-number k ranges in the interval $[-\pi, \pi)$, which is *not* a Brillouin zone for our (axially aperiodic) lattice. Figure 3.19 shows the dispersion relations for the stable structures in the lower panel of Figure 1.8,

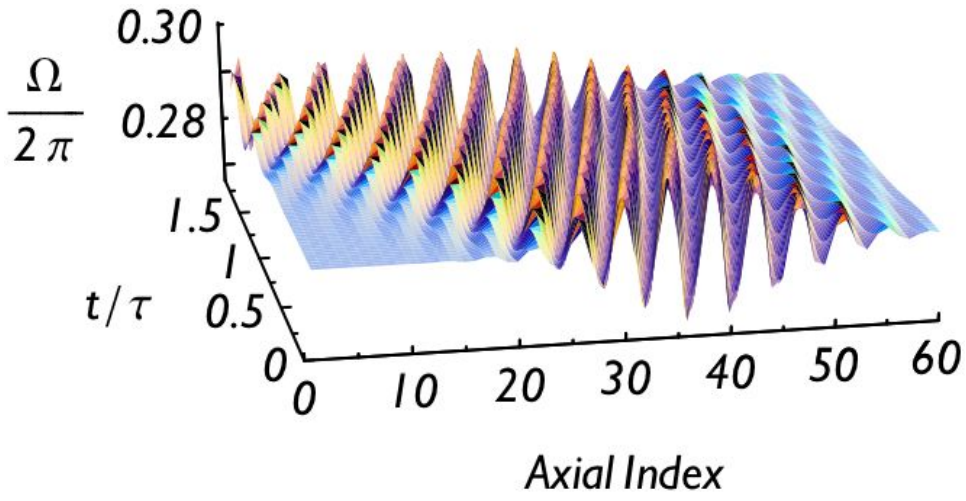

Figure 1.10. A wave-packet centered at $ka = 1.5$ for the structure with parastichy numbers $(3, 4)$.

truncating Equation (1.11) to 25 terms. The dispersion is highly non-monotonic outside of the long-wavelength acoustic regime. To gain insight into the origin of the multiple extrema, consider retaining only contributions from nearest neighbors, and label them so that $\omega_{j_1} j_1 > \omega_{j_2} j_2$. Since (j_1, j_2) are parastichy numbers for $\bar{\Omega}$, they are relatively prime. Therefore the dispersion relation in this approximation has no period smaller than 2π, but generally contains multiple local extrema. The nearest-neighbor approximation predicts the number of rotonic and maxonic extrema to be at most $2j_1 - 1$.

Rotons in helium are density fluctuations whose unusual dispersion relation has often been ascribed to an intrinsically quantum mechanical origin [43, 44]. By contrast, phyllotactic rotons are entirely classical and do not involve density fluctuations, since the particles have fixed axial positions. These rotons arise because nearest neighbors along the underlying one-dimensional spiraling Bravais lattice are not necessarily nearest neighbors in three-dimensional space: although increasing wave-vector drives particles nearby *along the spiral* increasingly out of phase, it can drive particles that are neighbors *in three dimensional space* more nearly into phase. An integration of the full equations of motion, shown in Figure 1.10, verifies rotonic behavior and demonstrates the dynamical stability of the lattice under small perturbations. While the group velocity is negative and the

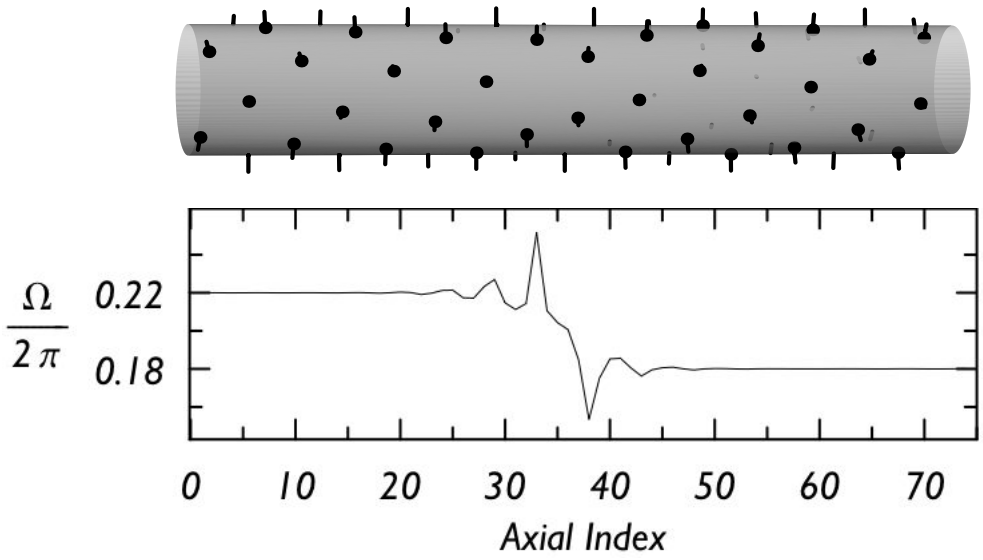

Figure 1.11. A kink between domains of parastichy numbers (4,5) and (5,6) as it appears on the physical cylinder and in a plot of the angular shift Ω versus the axial index.

profile moves backward, the phase velocity is clearly positive and the oscillations move forvard.

1.2.4 Kinks and Solitons

Thermodynamically, this highly degenerate one-dimensional system should be unstable towards domain-wall formation. To find the shape of these kinks we impose static step-like initial condition in a dynamical simulation and let them radiate energy in the form of traveling waves; when the resulting configurations are temporally averaged to remove residual oscillations and then used as new initial conditions, the resulting kink is static, as shown in Figure 1.11. These kinks are not particular to the dipolar interaction: simulations of cooled ion beams also show numerous kinks - apparently unnoticed up to now - in the outer ion shell [29, 32, 30, 31].

Our numerical study show that these kinks can travel and maintain shape as topological solitons. Since a kink separates domains of different screw angle, its motion must be accompanied by either phase slips or a uniform relative rotation of the two domains. The latter, adiabatic, motion is observed in all our numerical

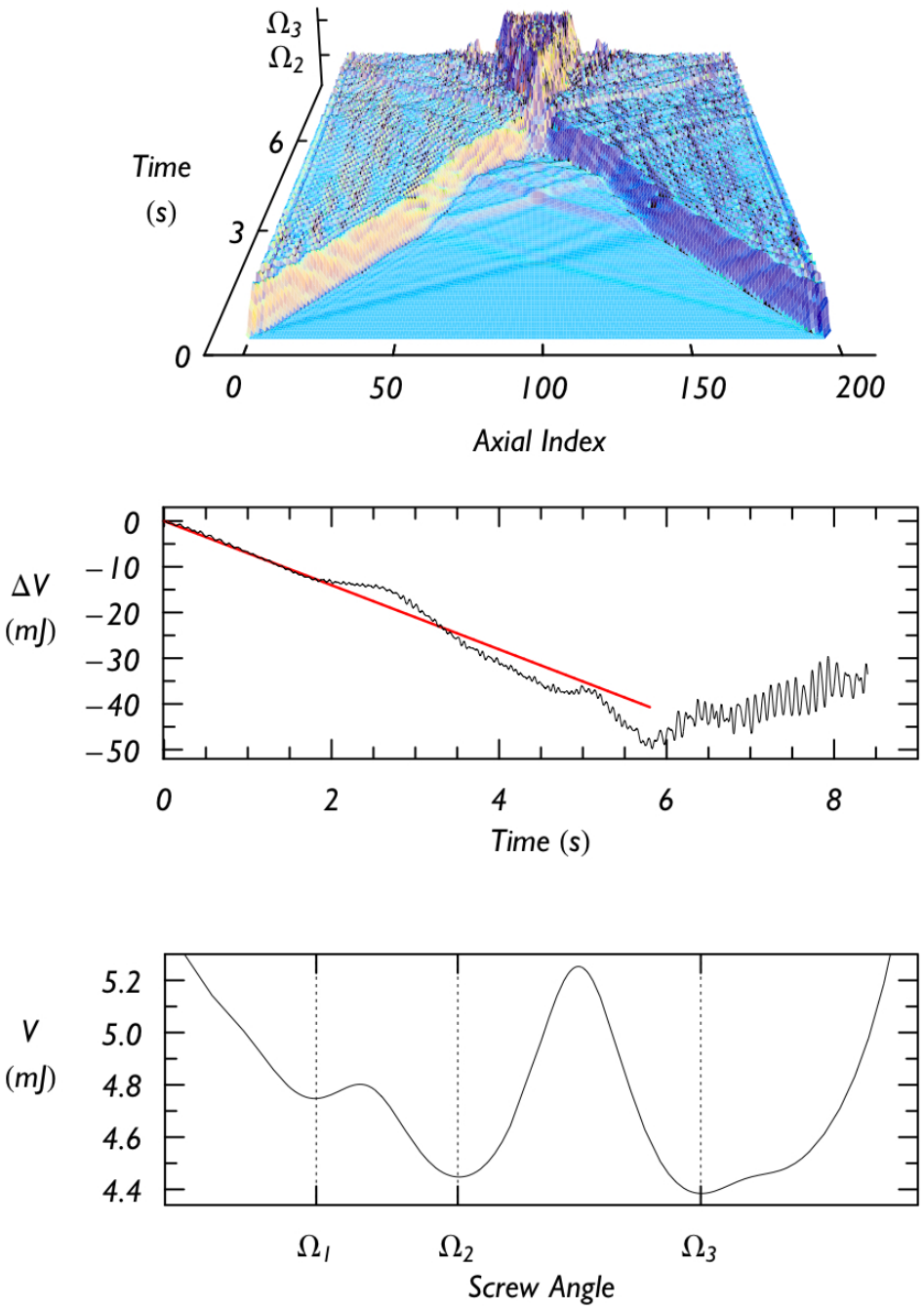

Figure 1.12. The collision of two solitons. For clarity, weak high-wave-vector phonons were smoothed by spatial averaging, here and in Figure 1.13. The potential energy V drops linearly as the lower-energy domains advance; deviations starting around $t = 2$ arise from interaction with elastic waves propagating in front of the solitons. The energy $V(\Omega)$ reflects an actual experimental apparatus of magnets and bearings, with $a/R = 0.7$ and minima at $\Omega_1/2\pi = 0.23$, $\Omega_2/2\pi = 0.28$, $\Omega_3/2\pi = 0.38$.

simulations.

Unlike other topological solitons such as the sine-Gordon variety, which can travel at any subsonic speed, here the speed of the kink, v_K, is tightly controlled by the dual constraints of energy conservation and phase matching at the interface between the two domains. Figure 1.12 shows a pair of solitons that form at the free ends of an initially stationary metastable structure Ω_1 in a low-density system with non-degenerate minima. As the solitons move toward each other, (preceded by elastic waves to ensure local angular momentum conservation), lower-energy domains of angle Ω_2 form in their wakes. The angular speed of the Ω_2 domains is $\dot{\theta} = v_K \Delta\Omega$, where $\Delta\Omega = \Omega_2 - \Omega_1$. Approximating the kink as a step, the time dependent energy is

$$E(t) = \left(I\Delta\Omega^2 v_k^2 - 2\Delta V\right) v_K t, \tag{1.12}$$

where $\Delta V > 0$ is the potential energy gained by a particle upon transfer from the outer (Ω_2) to the inner (Ω_1) domain [2]. Energy conservation then fixes v_K:

$$v_K^2 = \frac{2\Delta V}{I\Delta\Omega^2}. \tag{1.13}$$

For the simulation of Figure 1.12, the energy $V(\Omega)$ reflects an actual experimental apparatus of magnets and bearings, with $a/R = 0.7$ and minima at $\Omega_1/2\pi = 0.23$, $\Omega_2/2\pi = 0.28$, $\Omega_3/2\pi = 0.38$. The measured speed 22.1 s^{-1} agrees well with the value predicted from Equation 1.13, 23.4 s^{-1}.

More general simulations of interacting solitons exhibit a complex phenomenology [45]. Solitons can convert from one species to another upon collision, as seen at later times in Figure 1.12. At low densities, unstable domain boundaries can spontaneously fragment into pairs of counter-propagating solitons. Two different solitons moving in the same direction at different speeds can merge to form a third soliton.

Figure 1.13 demonstrates the latter phenomenon. Initial conditions are prepared so that two solitons emerge from an initial domain boundary. The left-hand soliton bounces off the free left-hand boundary, maintains its shape, and propagates rightward faster than the other. The two solitons then collide, merge and trans-

[2] Energy associated with elastic waves that precede the solitons must also be included in ΔV and $\Delta\Omega$.

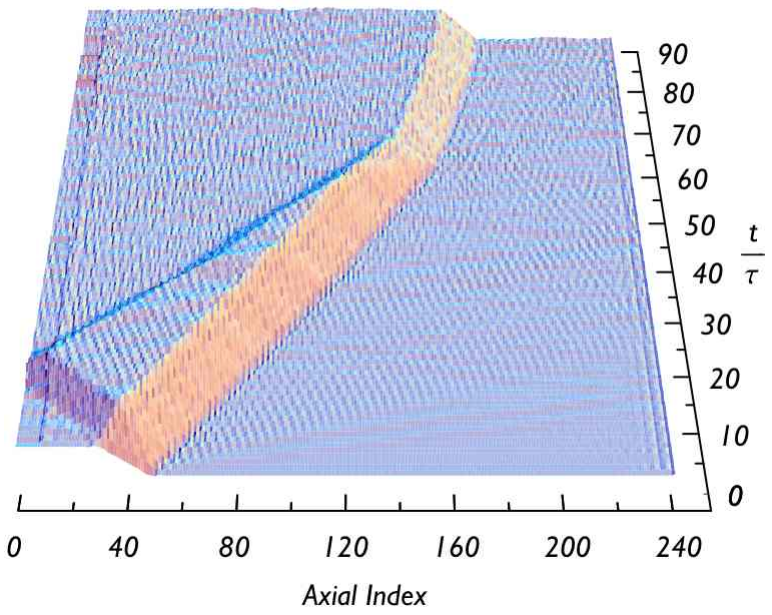

Figure 1.13. Fragmentation, reflection and merger of solitons for a system with $a/R = 0.15$, as in Figure 1.8.

form in a third soliton with a different characteristic speed. This set of behaviors is strikingly reminiscent of particle physics: like elementary particles, phyllotactic solitons can merge, split, decay and change identity upon collision. At sufficiently high temperature, they decompose into a sea of constituent particles. Both hadrons and phyllotactic solitons provide a family of quasi-degenerate, dynamically stable, composite objects. This similarity does not seem to rise beyond the level of a interesting analogy, however.

1.2.5 Applications

Since these results generalize to any long-ranged repulsive interaction, many cylindrically symmetric systems could support dynamical phyllotaxis. Cold atomic gases, with their extremely low dissipation, are particularly attractive. Adatoms [46, 47] or low-density electrons on non metallic carbon or boron nitride nanotubes could provide an example in condensed matter physics, and cooled particle beams provide an opportunity in particle physics. Colloidal particles in mesophase systems, which can self-assemble in cylindrical geometries [48], could provide a more strongly damped version, and constrained magnets [49] a macroscopic one.

A two-dimensional Wigner crystal forms when $r_s > 37$ [50]. To achieve phyllotactic degeneracy, $a/R = r_s^2/2R^2$ must be small enough. At $r_s = 37$, Equation 1.7 requires a minimal radius

$$R \geq \frac{37J}{2\sqrt{\pi}} a_0 \simeq 5.5J \text{ Å} \tag{1.14}$$

to generate a maximum peak rank J, with a_0 the Bohr radius for an appropriate effective mass and dielectric constant. When $a_0 = 0.53$ Å, the minimal degeneracy, $D = 2$ and $J = 2$, occurs for $R \simeq 11$ Å, a typical dimension for a carbon or boron nitride nanostructure. Axial relaxation of particle positions in a real Wigner crystal changes the particle density inside the kink, suggesting the possibility of charge transport via these solitons in a pinned crystal, if enough translational order survives [51].

1.3 A Continuum Model for the Phyllotactic Soliton

1.3.1 Topological Solitons in Physics

The topological soliton, the moving domain wall between degenerate structures, ubiquitously populates systems of discrete symmetry, most notably the Ising model, and appears at different scales and in many realms of physics [52]: in mechanical or electrical apparati [52, 53, 54], superconducting Josephson junctions [55], nonperturbative theory of quantum tunneling [56] and particle physics (e.g. Yang-Mills monopoles and instantons [57], sigma model lumps and Skyrmions [58]). We have shown that in phyllotaxis, different domains separated by topological solitons have different dynamics and store kinetic energy while rotating around the axis of the dynamical cactus. Moreover kinks among those domains have different shape, characteristic speed, behavior under collision.

Here we introduce a minimal, local, continuum model of the phyllotactic soliton and show how the effect of the kinetic energy can be subsumed into a modification of the potential energy, and the problem then solved in the familiar equivalent trajectory representation. The model predicts the speed of the solitons, trans-

fer of energy between boundaries, the observed screw angle shift, speed selection by boundaries conditions, and charge/density variations, and helps classify their zoology.

1.3.2 The Model

The dynamical cactus, a simple phyllotactic dynamical system depicted in Figure 2.2, consists of repulsive, massive objects holonomically constrained on rings rotating around a fixed axis: let $a = L/N$ be the distance between consecutive rings for a cylinder containing N objects, of length L and radius R, θ_i the angular coordinate of the i^{th} particle, and $\Omega_i = \theta_i - \theta_{i-1}$ the angular shift between consecutive rings. The total potential energy for unit length is

$$V = \frac{1}{2L} \sum_{i \neq j} U(\theta_i - \theta_j) \ , \tag{1.15}$$

where U is a long ranged repulsive interaction that makes the sum extensive and well-behaved, such as a dipole-dipole or a screened Coulomb.

We have shown that stable structures correspond to spiraling configurations: the energy of spiraling structures as a function of the screw angle ω is reported in Figure 1.8 for different values of a/R: as a/R decreases, commensurate structures become energetically costly, independent of the repulsive interaction used; for a/R low enough, any commensurate spiral of screw angle $\Omega = 2\pi\ i/j$ with i, j relatively prime becomes a local maximum, as the particle on the j^{th} ring becomes a nearest neighbor in the real space. The minima also become more nearly degenerate as the density increases, since for angles incommensurate to π each particle is embedded in a nearly uniform background charge from the other particles.

To describe domain walls between degenerate structures we propose the following minimal model: in the continuum limit $i \to z$, $\theta_i \to \theta_z$, the screw angle is now $\omega_z \equiv \partial_z \theta$.

We introduce the minimal (linear density of) Lagrangian

$$L = \frac{1}{2} I \dot{\theta}^2 - V(\partial_z \theta) - \frac{\kappa}{2} \left(\partial_z^2 \theta \right)^2 . \tag{1.16}$$

The first term of Equation 1.16 is the kinetic energy ($I \equiv \mathcal{I} a^{-1}$, $\mathcal{I}$ being the

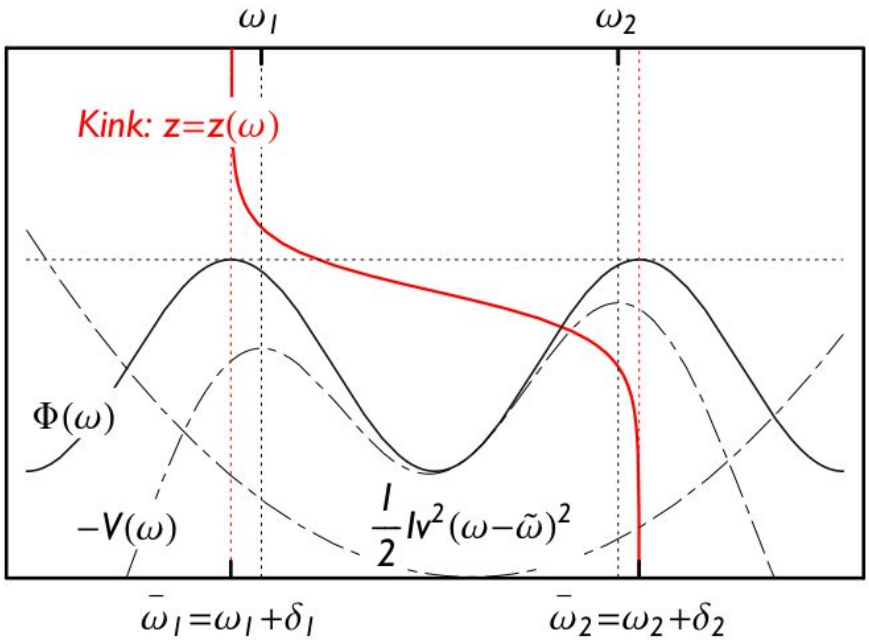

Figure 1.14. In the equivalent Newtonian picture, the soliton corresponds to the space-time diagram of a particle that starts and ends in two maxima of the potential energy $\Phi(\omega) = \frac{1}{2}v^2 I(\omega - \tilde{\omega})^2 - V(\omega)$. The figure shows the dependence of the boundary conditions $\bar{\omega}_{1,2}$ from v, $\tilde{\omega}$.

moment of inertia of a ring), the second accounts locally for the potential energy, the last conveys the rigidity toward spacial variations of the screw angle. The equation of motion follows from Equation 1.16,

$$I\partial_t^2\theta = \partial_z V'(\partial_z\theta) - \kappa\,\partial_z^4\theta, \tag{1.17}$$

and corresponds to angular momentum conservation.

1.3.3 The General Solution

Whatever the precise form of the actual interaction and the geometric parameters of the problem, the existence of solitonic solutions can be shown and many quantitative results achieved by reducing the problem to an equivalent Newtonian one.

We seek a traveling solution of the form

$$\theta = \theta(z - vt) + wt, \tag{1.18}$$

with w accounting for angular rotation invariance. From $\partial_t^2\theta = v^2 \mathrm{d}^2\theta/\mathrm{d}s^2$, with $s = z - vt$ one obtains the equivalent Newtonian equation

$$\kappa \frac{\mathrm{d}^2\omega}{\mathrm{d}s^2} = -\Phi'(\omega). \tag{1.19}$$

with κ being the equivalent mass, the equivalent potential Φ given by

$$\Phi(\omega) = \frac{1}{2} v^2 I(\omega - \tilde{\omega})^2 - V(\omega), \tag{1.20}$$

with $\tilde{\omega} \equiv \tau/(Iv^2)$, and τ a constant to be determined, with the dimension of a torque[3].

Equation 1.19 shows that solitonic solutions correspond to Newtonian trajectories between two equally valued local maxima of the equivalent potential energy Φ. When $v \neq 0$, these in general do not correspond to ω_1, ω_2, the stable structures of V, but are located in $\bar{\omega}_1 = \omega_1 + \delta_1$, $\bar{\omega}_2 = \omega_2 + \delta_2$ (see Figure 1.14): this shift is observed in dynamical simulations, in the form of an elastic wave propagating at the speed of sound in front of the soliton, as in Figure 1.15. The physical origin of this shift is related to momentum conservation: when propagating the soliton changes the angular momentum of the new domain. The shift from ω to $\bar{\omega}$ allows momentum conservation by providing a torque $-\frac{\mathrm{d}V(\bar{\omega})}{\mathrm{d}\omega} \neq 0$. We will return on this later.

In summary, we have a kink only when the following system of equations is satisfied.

$$\begin{cases} \Phi'(\bar{\omega}_1) = \Phi'(\bar{\omega}_2) = 0 \\ \Phi(\bar{\omega}_1) = \Phi(\bar{\omega}_2). \end{cases} \tag{1.21}$$

For a static soliton, the equations of existence 1.21 reduce to

$$\begin{cases} \tau = V'(\bar{\omega}_1) = V'(\bar{\omega}_2) \\ \tau(\bar{\omega}_1 - \bar{\omega}_2) = V(\bar{\omega}_1) - V(\bar{\omega}_2). \end{cases} \tag{1.22}$$

[3]For static solitons it is easier to work in terms of τ, for dynamical ones in terms of $\tilde{\omega}$.

The first line in the System 1.22 tell us that τ is an applied torque, while the second line shows that no torque is necessary if the structures are degenerate: unlike topological solitons of the sine-Gordon-like class, here static solutions between non degenerate domains are allowed, through an applied torque that shifts the two structures out of the minima of V. Unlike the sine-gordon-like one, our Lagrangian is not invariant under Poincaré transformations, and the traveling soliton is not just a boost transformation of the the static one: in particular the shifts increases with $\delta_1,\ \delta_2 \propto v^2$ (Equation 1.20, Figure 1.14).

Depending upon the choice of w, as the soliton travels along the axis, the two domains rotate; because they are shifted from equilibrium, energy flows through the boundaries of the system. By requesting no energy accumulation in the kink we fix w in $\theta = \theta(z - vt) + wt$. The power entering the system at the asymptotic boundaries can be deduced via the Noether theorem, to be

$$j_\infty = -V'(\omega)\partial_t\theta, \tag{1.23}$$

the torque times the angular speed, not surprisingly. By requesting $j_{+\infty}$=$j_{-\infty}$ one then finds

$$w = v(\bar{\omega}_1 + \bar{\omega}_2 - \tilde{\omega}). \tag{1.24}$$

That fixes w and thus the angular velocities of the domains as a function of $\bar{\omega}_1$, $\bar{\omega}_2$, v.

1.3.4 Predicting Numerical Data

In the experimental settings and in dynamical simulations, the dynamical cactus with free boundaries was seen expelling higher energy domains through a soliton. Free boundaries implies $j_{\pm\infty} = 0$. From Equation 1.23, since V' cannot be zero on both boundaries, nor can $\partial_t\theta$, we have only one possible free boundaries solution between non degenerate structures $V(\omega_1) < V(\omega_2)$: it has $\delta_1 = 0$ (and thus $\bar{\omega}_1 = \omega_1$), $\delta_2 \neq 0$ (and thus $\bar{\omega}_2 = \omega_2 + \delta_2$), and from Equation 1.24 we obtain $w = \bar{\omega}_2$. Equations 1.21 fix the speed to

$$v^2 = \frac{2\Delta\bar{V}}{I\Delta\omega^2} \tag{1.25}$$

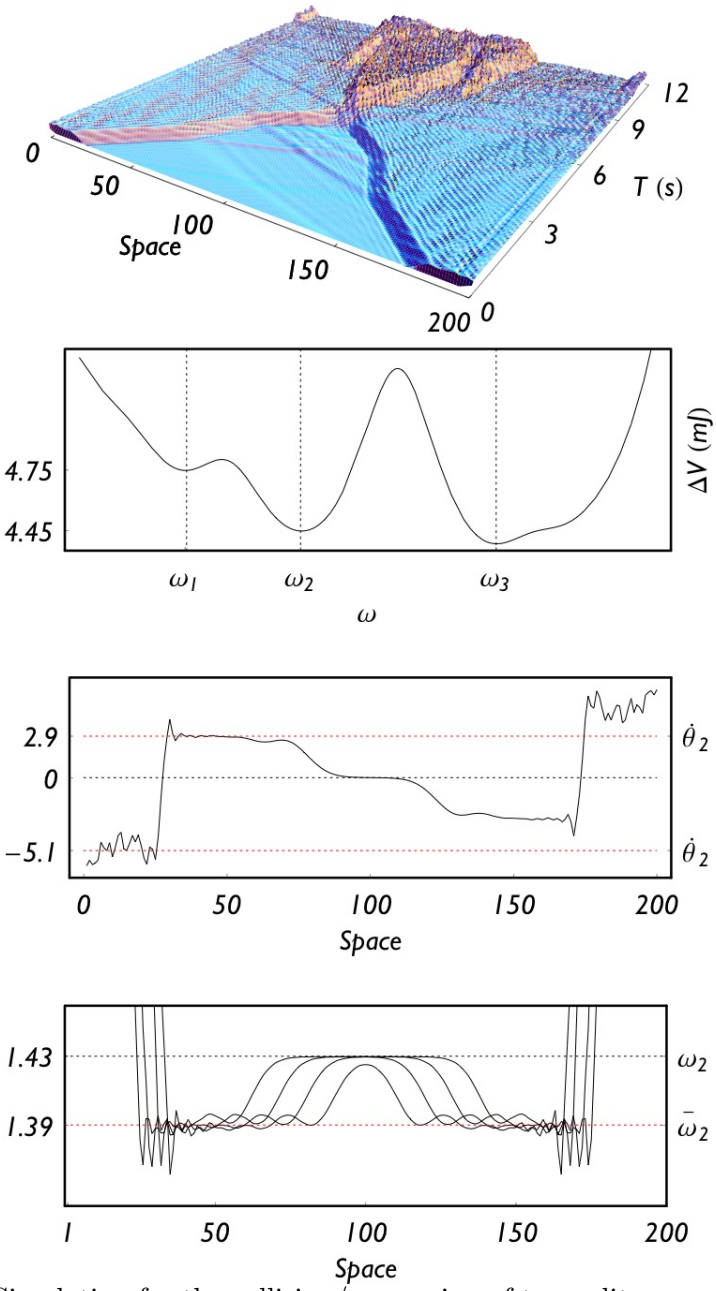

Figure 1.15. Simulation for the collision/conversion of two solitons on the *real* dynamical cactus, emitted from free boundaries. Top: screw angle *vs.* space and time. Second panel: energy per particle (mJ) *vs.* screw angle (rad)for our system ($\omega_1 = 1.79$ rad, $\omega_2 = 1.43$ rad, $\omega_3 = 2.40$ rad). Third panel: angular speed (s^{-1}) *vs.* space at a given time: the speed of the soliton can be extracted to $v = \Delta\dot{\theta}/\Delta\omega = 22.1\ s^{-1}$ (predicted $24.3\ s^{-1}$). Predicted shift in screw angle $\delta_2 = \omega_2 - \bar{\omega}_2 = -0.043$ rad, agrees excellently with numerical observations (Bottom: plot of the screw angle *vs.* space at different times while the soliton and its preceding wave advance).

with $\Delta\bar{V} = V(\bar{\omega}_1) - V(\bar{\omega}_2)$. By expansion of V around ω_2, $V \simeq \frac{1}{2}Ic^2(\omega - \omega_2)^2$, ($c$ is speed of sound in the domain ω_2), we obtain the shift

$$\delta_2 = \Delta\omega \frac{v^2/c^2}{1 - v^2/c^2}. \tag{1.26}$$

Since $w = \bar{\omega}_2$, the region of lower energy rotates uniformly, while that of higher energy, which is shifted, remains still: since there is no energy flow through the boundaries, the kink transforms the potential energy difference between the two domains in the kinetic energy of rotation – and vice versa, depending on its direction of propagation. Figure 1.15 shows results from a dynamical simulation of the *real* dynamical cactus: solitons start on the free boundaries in a higher energy domain as a lower energy domain expands inside, preceded by a torque that accommodates the shift δ_2. From the angular velocities of the domains (Figure 1.15 third panel) a speed of 22.1 s^{-1} can be extracted, and compared with the value 23.4 s^{-1} predicted by Equation 1.25: the drop is likely due to energy dissipation into phonons – a known effect on other discretized solitons. The predicted shift $\delta_2 = -0.043$ rad of Equation 1.26, is in excellent agreement with the simulation (Figure 1.15, last panel).

Even without knowledge on the precise form of V, a few considerations can be made on asymptotic states of the collisions: the domains beyond the approaching pair of kink anti-kink rotate with opposite angular velocity $\dot{\theta} = v\Delta\omega$, v given by Equation 1.25. After collision v changes sign and so must $\Delta\omega$: the emerging asymptotic configuration must be that of a pair of different kink anti-kink, connecting the old asymptotic domain with a different nearest neighbor, hence collision metamorphosis. After collision v, w will need to be different in order to satisfy Equations 1.21. Difference in w implies a shift δ_1 and thus a torque wave. Since the new domains are closer in energy, the new speed is also lower.

1.3.5 Solitons Among Degenerate Structures

To investigate the degenerate case, typical of high R/a ratios, we consider for simplicity a symmetric potential V, as in Figure 1.16; symmetry requires now $\tilde{\omega} = (\omega_1 + \omega_2)/2$, and both boundaries are equally shifted in opposite directions under torque of intensity $|\tau| = \frac{I}{2}v^2(\bar{\omega}_2 - \bar{\omega}_1)$ (Equations 1.21). Not unlike the

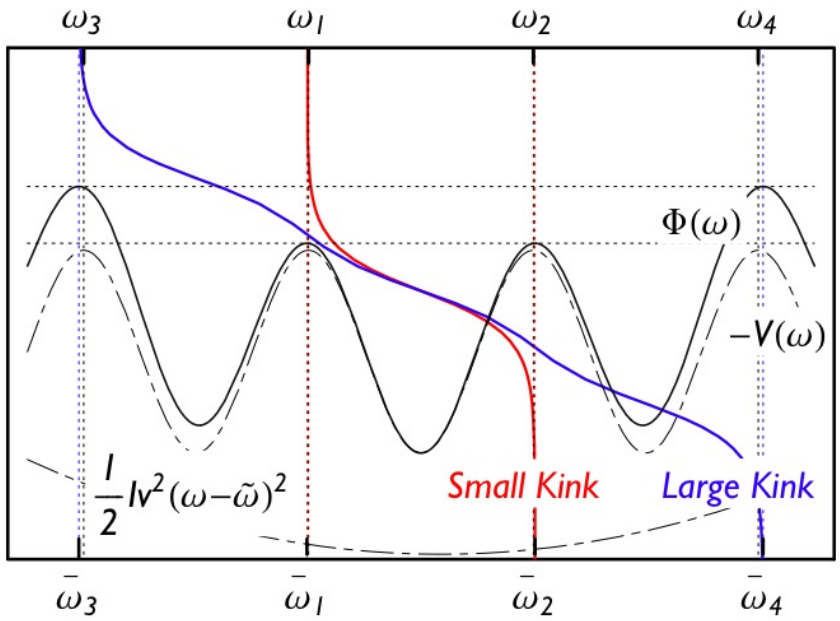

Figure 1.16. Equivalent Newtonian diagram for symmetrical solitons. Solitons with the same speed, but connecting different domain are possible under different applied torque.

sine-Gordon soliton, the symmetric soliton becomes shorter as v increases: the maximum velocity of the trajectory of the equivalent newtonian problem in Figure 1.14 increases as the equivalent potential difference between the maximum and the bottom of the pit does; in the real picture, this corresponds to a shortening of the soliton.

Equation 1.24 tells us that the two domain rotate in opposite direction with angular velocity

$$|\dot{\theta}| = v(\bar{\omega}_2 - \bar{\omega}_1). \tag{1.27}$$

The system inverts rotation while transmitting power

$$\tau\dot{\theta} = Iv^3\Delta\bar{\omega}^2/2 \tag{1.28}$$

along the tube.

For any given velocity, many solitons between degenerate structures are allowed, corresponding to different applied torques, as in Figure 1.16. With the same torque τ at the boundaries, by adiabatic increments of angular speed one could perhaps

transform the soliton into shorter and shorter ones.

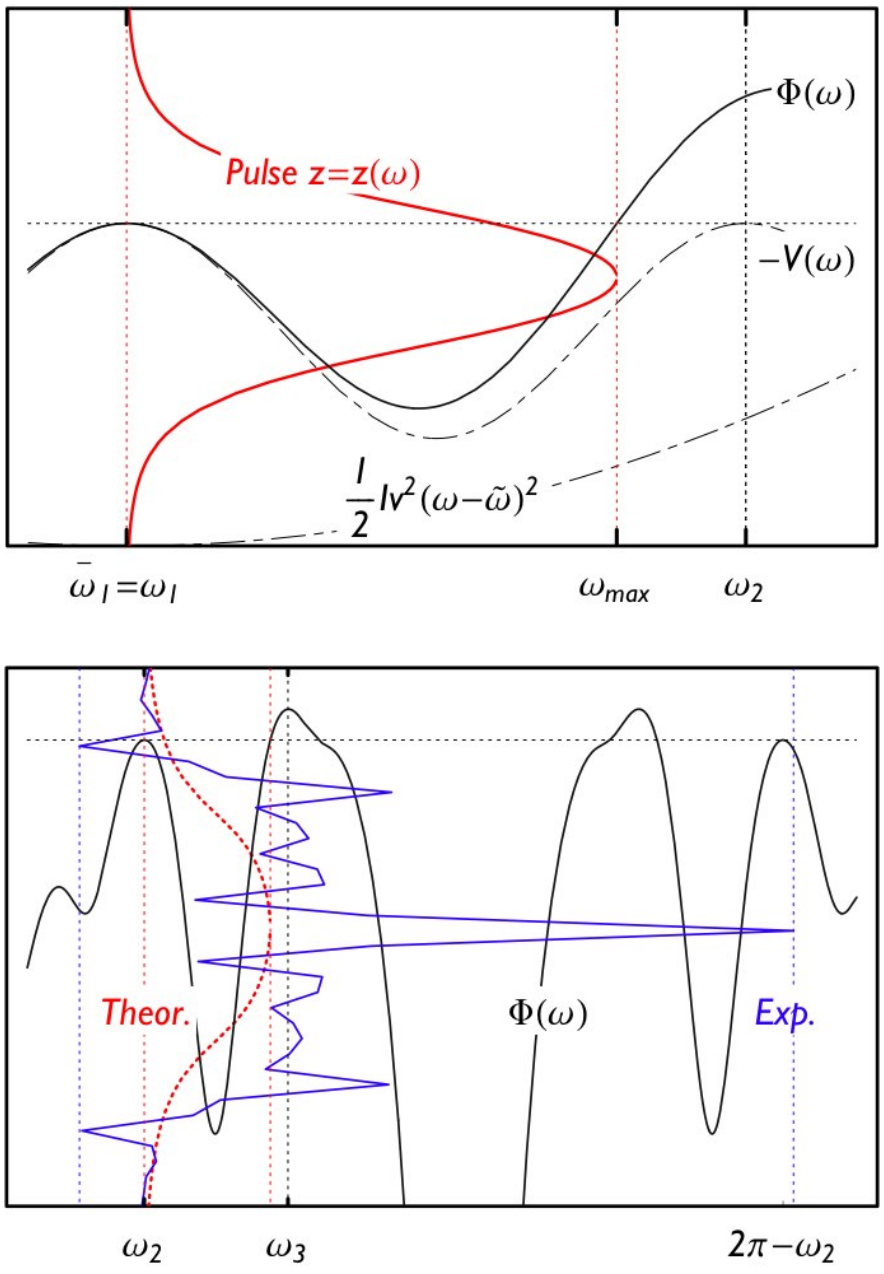

Figure 1.17. Top: a traveling pulse among degenerate structures is possible because of the non-zero speed v. Bottom: theoretical (red dashed) and experimental (blue solid) "frozen-in" pulse on the energy curve of the dynamical cactus.

1.3.6 Pulses

The equation of motion also predicts pulses, both dynamic and static (frozen-in). The top panel of Figure 1.17 shows the pulse soliton in the equivalent Newtonian picture as a trajectory falling from a local maximum of Φ, say ω_1, and coming back after hitting an higher potential barrier, before reaching the neighboring $\bar{\omega}_2$. Clearly pulses posses less inertia, since only the region occupied by the pulse rotates during propagation.

These pulses can propagate with free boundaries and no applied torque is necessary – although solutions corresponding to different boundary conditions can be found as well by choosing $\tilde{\omega} \neq \omega_1$. For high values of the speed v, pulses might involve more than one neighboring structure; the speed of sound is the upper limit for the velocity, (not unlike kinks in the sine-Gordon class): for $v > c$ the maximum of Φ around ω_1 becomes a minimum and the oscillating equivalent newtonian trajectory corresponds to vibrations around the stable configuration.

As v decreases three things can happen.

- If $V(\omega_1) < V(\omega_2)$, as v approaches from above the value given in Equation 1.25, the pulse stretches into a pair of kink and anti-kink (between domains ω_1 and $\bar{\omega}_2$) posed at infinite distance from each others, moving at the same speed in the same direction.

- If $V(\omega_1) = V(\omega_2)$, as $v \to 0^+$, the pulse tends to a infinitely spaced static kink and anti-kink pair.

- If $V(\omega_1) > V(\omega_2)$, as v goes to zero the pulse freezes in into a static one.

It is still an open question whether a frozen-in pulse could breath.

Dynamical simulations of the dynamical cactus confirm the presence of moving pulses. In the absence of applied torque, theory predicts that frozen-in pulses exist only in structures of locally higher energy; pulses were observed experimentally in the magnetic cactus apparatus, in higher energy domains as shown in Figure 1.17, bottom. We speculate that they arised from a kink-antikink symmetric collision.

1.3.7 Density Variations

We have already discussed how Wigner crystals of electrons on large semiconducting tubes are candidate environments for the phyllotactic soliton at nanoscale. A crystal pinned by the corrugation potential and/or impurities will not slide along the tube under a weak enough external field.

We can extend the continuum model to incorporate variations in the linear density to investigate the possibility of charge transport by the soliton. Let $\zeta = \mathrm{d}z/a$ be the relative axial displacement, and rescale the interaction

$$V(z) \to \left(\frac{\lambda(z)}{\lambda_o}\right)^2 V(z), \tag{1.29}$$

where λ and $\lambda_o = N/L$ are the linear density in presence and absence of axial

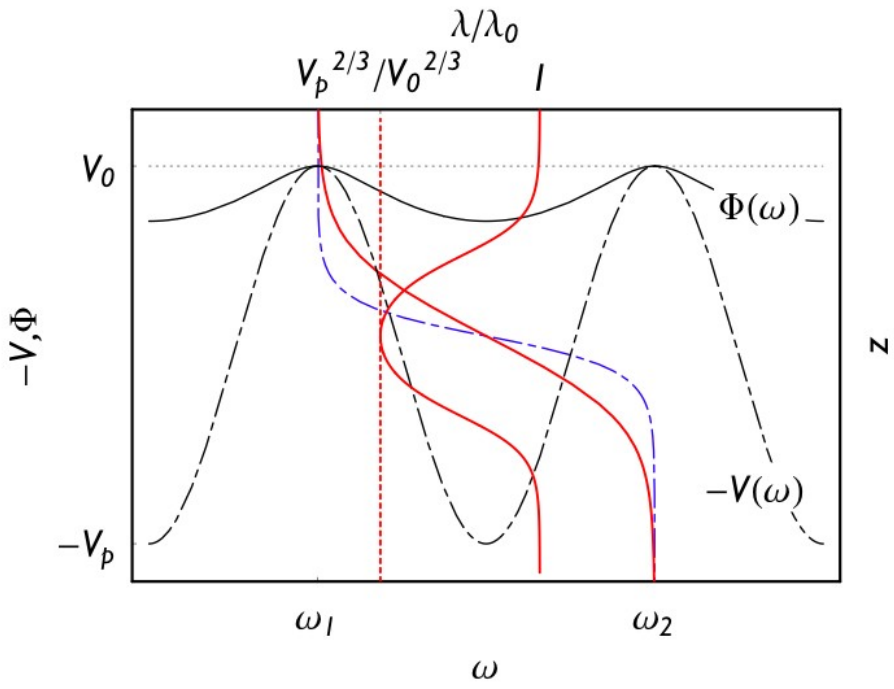

Figure 1.18. Equivalent Newtonian diagram for an axially unconstrained soliton. In blue, dashed, the axially constrained soliton among the stable structures ω_1, ω_2. In red, solid, the axially unconstrained one – which is longer – and the drop in density λ corresponding to the soliton.

displacement respectively: then

$$\frac{\lambda(z)}{\lambda_o} = \frac{1}{1 + \partial_z \zeta(z)}. \tag{1.30}$$

Sparing the details of the calculations, in the long tube approximation we find for the density of a static soliton (kink or pulse)

$$\frac{\lambda(z)}{\lambda_o} = \left(\frac{V_o}{V\left(\bar{\omega}\left(z\right)\right)} \right)^{2/3} \tag{1.31}$$

where V_o is asymptotic value of V and the static soliton $\bar{\omega}(z)$ is the the solution of the equivalent Newtonian Equation 1.19 with potential

$$\Phi\left(\omega\right) = -V_o^{2/3} V\left(\omega\right)^{1/3}. \tag{1.32}$$

$f = 2V_0$ is the force exerted at the boundaries. $V^{1/3}$ and V have the same set of locally minimizing arguments and the same ordering among their local minimum values: the extension to axial displacements does not alter any of the conditions for existence of kink and pulse solitons, as given by Equations 1.21. Equation 1.31 shows a drop in density in correspondence with the soliton, and thus, for a Wigner crystal of electrons, a net positive charge is found:

$$Q = \frac{e\lambda_o\sqrt{\kappa}}{\sqrt{2}m_e V_0^{1/3}} \int_{\omega_1}^{\omega_2} \sqrt{V^{1/3}\left(\omega\right) - V_0^{1/3}} \times \frac{\left(V_o^{1/3} + V^{1/3}\left(\omega\right)\right)}{V^{2/3}\left(\omega\right)} \mathrm{d}\omega \tag{1.33}$$

(e, m_e are the electron charge and mass).

In conclusion a continuum model for the phyllotactic soliton leads to good agreement with numerical data, provides a tool for calculations of otherwise elusive quantities, as charge and energy, and could be used in the future to develop its thermodynamics: since kinks can be seen as thermal excitations, their density, and thus the density of charge carriers in a cylindrical Wigner crystal can be calculated as a function of temperature.

Chapter 2

Ground State Lost, Degeneracy Found: Artificial Spin Ice

2.1 Water Ice, Square Ice, Spin Ice

Disordered states are complex and often do not reveal themselves completely to experiment. In neural networks, structural glasses, economic models and countless other systems, disorder is often associated with frustration, a competition between interactions, not all of which can be satisfied. Frustrated systems have been the subject of extensive research due to their unusual statistical mechanics and the availability of good materials systems for experimental study.

Historically, the first identified frustrated system was crystalline Ice, which showed disorder and thus entropy at very low temperature. Back in the thirties, Giaque *et al.* computed the entropy change in water by integrating the measured specific heat

$$\Delta S = \int_{T_1}^{T_2} \frac{C(T)}{T} \mathrm{d}T \tag{2.1}$$

between the liquid helium temperature and the gas phase. They compared their result with the calculated absolute entropy for the gas phase using spectroscopic measurements of energy leels of water molecules, and found a difference, a residual entropy [9]. To interpret this striking fact they assumed at first that the ice was not completely equilibrating.

As Pauling showed [11], water ice is indeed equilibrated, yet its ground state

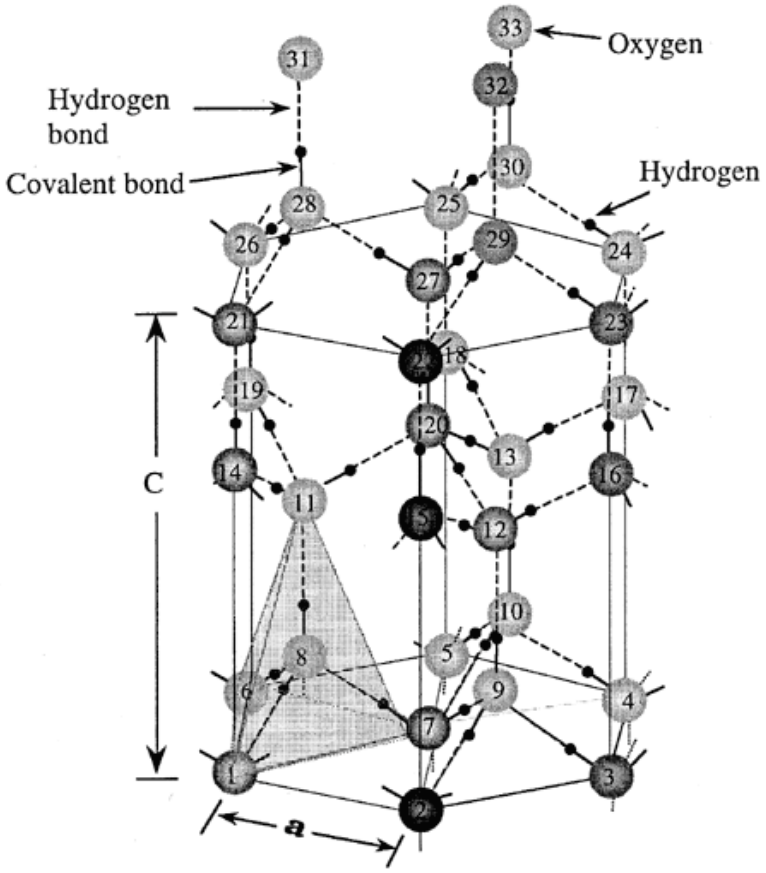

Figure 2.1. Figure 1: A schematic of the crystal structure of hexagonal ice Ih. Each H_2O molecule has its four nearest neighbors arranged near the vertices of a regular tetrahedron (shaded) centered about the molecule of interest. The stacking sequence is . . . ABBAABBA . . . and may be seen from the numbers on the oxygen atoms: numbers 1-7 = A, 8-10 = B, 11-13 = B, 14-20 = A, 21-27 = A, 28-30 = B, 31-33 = B. Near the melting point the O-O distance is 0.276 nm, and the lattice parameters are a = 0.4523 nm and c = 0.7367 nm (from Shulson [10]).

is an extensively degenerate manifold which returns a residual entropy [1]. Water Ice can have many structures, but in its most common terrestrial form (lh ice) water freezes in a hexagonal lattice, where each H_2O molecule has four nearest neighbors in a tetrahedral arrangement. The oxygen atom of each molecule is strongly covalently bonded to two hydrogen atoms, while the molecules are weakly hydrogen bonded to each other [10]. Consider each oxygen atom as the center of a

[1]It is interesting to contrast this with the case of our square artificial spin ice, which instead has a non degenerate, well defined (up to spin flip) ground state, yet after demagnetization returns an extensively degenerate manifold. We will return on this later.

vertex with four oriented links representing the bonds with an hydrogen atom, their orientation pointing toward or away from the oxygen atom if the bond is hydrogen or covalent respectively. Each vertex can have only two bonds pointing in and two pointing out, since each oxygen atom must be bound covalently to two hydrogen atoms, as in Figure 2.1. Pauling demonstrated that these degrees of freedom in the accommodation of the hydrogen bonds leads to extensive degeneracy, and thus to a residual entropy [11].

Since then, the two-in/two-out Ice Rule has been studied extensively. Pauling only gave an estimate of the extensive degeneracy of water ice ($D = (3/2)^{N/2}$), but the exact partition function has been calculated for simplified two dimensional square lattices [59, 60, 61]. These models, called vertex models, include, yet do not reduce to, "square ice": each vertex has 16 possible configurations; the general 16-vertex model attributes a certain energy to every given vertex type; square ice assigns the lowest (zero) energy to vertices that obey the two-in/two-out, rule.

Water Ice can be considered a frustrated system: interpreting every link, or bond, as an "interaction", only two interactions can be satisfied. In recent years a new class of frustrated magnetic materials ($Ho_2Ti_2O_7$, $Dy_2Ti_2O_7$, $Ho_2Sn_2O_7$) has been identified, in which the low temperature disorder can be described by the ice rule. In this spin ice materials, the spin configuration mimics the frustration of hydrogen positions in water ice [62, 63].

Spin Ice materials have revived interest in the experimental research in residual entropy, after a time when an enormous boost in theory was frustrated by the lack of experimental accessibility. Indeed, pure crystals of water ice are particularly hard to create, while depending on the material used in a spin ice, it is generally much easier to create large single crystals of spin ice materials than the corresponding water ice materials. Additionally, the interaction of a magnetic field with the spins in a spin ice material make spin ice materials much nicer materials for examining residual entropy than water ice.

As a practical matter, however, individual spins within a material are difficult to probe experimentally without altering the state of the system. One way around this problem is to create a frustrated system in which the individual elements can be directly probed.

In collaboration with the research group of Peter Schiffer we have developed

and studied an artificial frustrated system, which is governed by a "quasi-ice rule". The artificial spin ice demonstrates that artificial frustrated magnets can provide a rich new arena in which to study the physics of frustration.

2.2 Artificial Spin Ice

2.2.1 The Idea

Dr. P. Schiffer thought that frustration could be studied by means of an artificial array of magnetic nanoislands: a two-dimensional lattice of elongated permalloy islands with the long axes of the islands alternating in orientation along the two principal directions of the array lattice. This island size was to be sufficiently small that the atomic spins were ferromagnetically aligned in a single domain (as demonstrated below), but large enough that the moment configuration was stable at 300 K; islands would interact magnetically.

We soon realized that, although the magnetic interaction was long-ranged, the problem could provide an artificial physical realization of a two-dimensional vertex model. An hexagonal lattice would be the ideal candidate for a vertex model that provides an extensively degenerate ground state manifold, since all the three islands converge on a vertex with the same angle, thus yielding the same magnetic interaction. All the vertices except two excited ones (those with all magnetic moments pointing out or in) would have the same energy. At first fabrication problem prevented realization of this hexagonal geometry (although the arrangement was later realized and we are currently studying it) and thus we resorted to a square lattice.

R. F. Wang and collaborators in Schiffer's group performed experiments on arrays with lattice parameters ranging from 320 nm to 880 nm, with a fixed island size (80 nm x 220 nm laterally and 25 nm thick). The moment of each island was approximately 3 10^7 Bohr magnetons (estimated from the known magnetization of permalloy), and the magnetic field from an island was of order 10 Oe at the center of nearest neighbor islands – leading to an interaction energy of order $10^4 K$ between nearest neighbors. The magnetocrystalline anisotropy of permalloy is effectively zero so that the shape anisotropy of each island (the self-energy of the

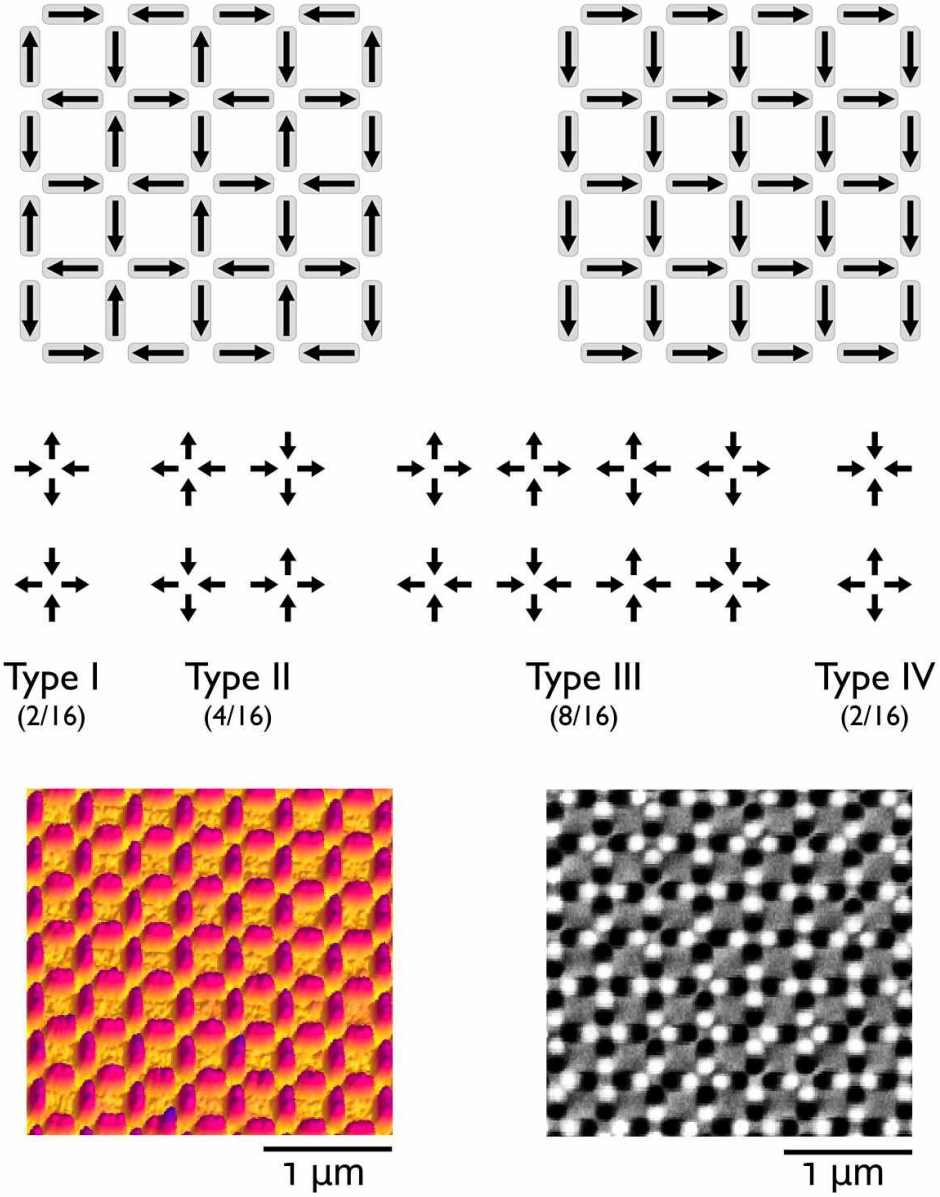

Figure 2.2. The artificial spin-ice lattice of [64]. The demagnetized tiling of the ground state (top left) and a fully polarized tiling of type-II vertices (top right). The sixteen possible vertices of artificial spin ice and their multiplicities (middle). Atomic force (bottom left) and magnetic force (bottom right) microscope images of the experimental system.

islands magnetic moment, which is controlled by its shape) forced its magnetic moment to align along the long axis, thus making the islands effectively Ising-like.

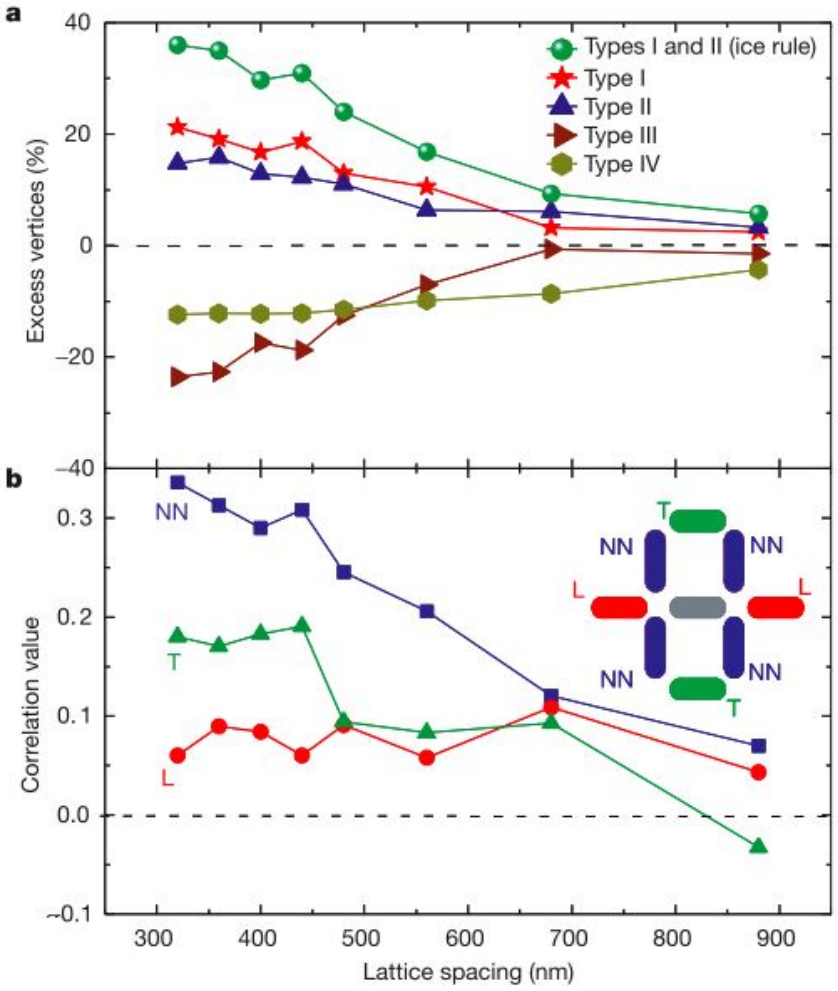

Figure 2.3. Statistics of moment configurations, obtained from between 1,000 and 3,000 islands in combined measurements of 2-4 different arrays for each lattice spacing. a. The excess percentages of different vertex types, plotted as a function of the lattice spacing of the underlying square array lattice. Note that the excess percentages approach zero for the largest lattice spacing. b. The correlations between different pairs of the islands as a function of the lattice spacing of the underlying square lattice. The inset shows our definitions of the near neighbor pairs from the grey central island. For both the correlations and the vertex statistics, the typical variation between images for nominally identically prepared samples was $< 10\%$ for the closely spaced lattices in which we had more than 1,000 islands in a single image, but up to 50% for the more widely spaced lattices in which we had only a few hundred islands per image.(from [64]).

For the vertex as a whole, there are four distinct topologies for the configurations of the four moments with a total multiplicity of 16, as shown in Figure 2.2. We label the configurations I - IV in the order of increasing magnetostatic energy,

but no configuration can minimize all of the dipole-dipole interactions (even type I only minimizes the energy for four of the six pairs in a vertex), and thus the system is frustrated. However this array actually has a single ground state, unique up to a global spin flip, that carries no macroscopic moment, shown in Figure 2.2.

The system was demagnetized by first fully polarizing it in a large external field and then gradually decreasing the field in an alternating stepwise fashion while rapidly rotating the sample, all at room temperature. The field magnitude is reduced from 1308 Oe to zero in steps of 32 Oe while its polarity alternates in the lab frame, with a sweep rate of 24000 Oe/second and a hold time of one second at each field value. The sample rotates at 1000 RPM. The magnetic moment of a single island, 80 $\times$ 220 $\times$ 25 nm thick, is $\sim 3 \times 10^7 \mu_B$.

Magnetic force microscopy (MFM) allows to image the orientations of all of the moments in a large area (10x10 microns), far from the edges of the arrays (Figure 2.2). From the MFM data, the moment configuration of the array can be determined, and the many vertex types directly observed in the actual system.

It is interesting to compare the vertex populations in the demagnetized arrays with the purely random results. We compute the excess percentage for each type of vertex, defined as the difference between the percentage observed and that expected for a random distribution. We plot this excess versus lattice spacing in Figure 2.3 for each of the four vertex types, as well as for types I and II combined. The excess percentage of vertices with a two-in/two-out configuration (types I and II) was well over 30% for the smallest lattice; in other words, over 70% of all vertices had a spin-ice-like configuration. This excess percentage decreased monotonically with increasing lattice spacing (decreasing interactions), approaching zero for our largest lattice spacing, as would be expected for non-interacting (randomly oriented) moments. In fact, the excess for all vertex types approached zero as the lattice spacing increased, lending credence both to our understanding of the system and to the effectiveness of the rotating-field method in enabling facile local re-orientation of the moments.

We define a correlation C, such that C = +1 if two moments are aligned to minimize the dipole interaction energy, and C = -1 if two moments are aligned to maximize the dipole energy, if the moments for a particular type of neighboring pair were uncorrelated on the lattice, the average value of C would be zero. We

found no long range correlations beyond the L (longitudinal next nearest) and T (transverse next nearest) neighbors (see Figure 2.3). Stronger correlations are found for nearest neighbors NN, and surprisingly L is lower than T.

2.3 Effective Thermodynamics of Artificial Spin Ice

2.3.1 The Problem

Although the resulting magnetic states in the artificial spin ice experiments had only a small residual moment and a much lower energy than the fully polarized starting configuration, the unique ground state was never reached, nor even closely approached. Yet the demagnetization protocol returns coherent statistics between successive runs, at the same lattice constant, in what seems to be a well defined state. How to identify it ?

2.3.2 The Vertex Model

Before measurement with magnetic force microscopy, the experimental system undergoes a rotational demagnetization which produces a disordered configuration of the island moments with very small net magnetization, locally and globally. Therefore long-range magnetic interactions are weak and do not sum coherently. The dominant interactions within the array connect the nearest-neighbor islands that comprise a given vertex.

We describe our system as a 16-vertex model [60, 61], with the vertices of Figure 2.2. The mutual magnetostatic energy of the four islands comprising a given vertex is written as $E_{\rm I}$, $E_{\rm II}$, $E_{\rm III}$ or $E_{\rm IV}$ and is denoted as a "vertex energy". All vertex energies are calculated with fully relaxed micromagnetic simulations of isolated vertices using the Object Oriented MicroMagnetic Framework (OOMMF) project at ITL/NIST [2]. For simplicity, we set $E_{\rm I} = 0$. For the arrays studied, the vertex energies maintain the relative order $E_{\rm I} < E_{\rm II} < E_{\rm III} < E_{\rm IV}$ with a typical energy scale $E_{\rm II} - E_{\rm I} \sim 2 \times 10^5$ K ($\sim$ 3 attojoules) at a lattice constant of 320 nm.

[2] http://math.nist.gov/oommf

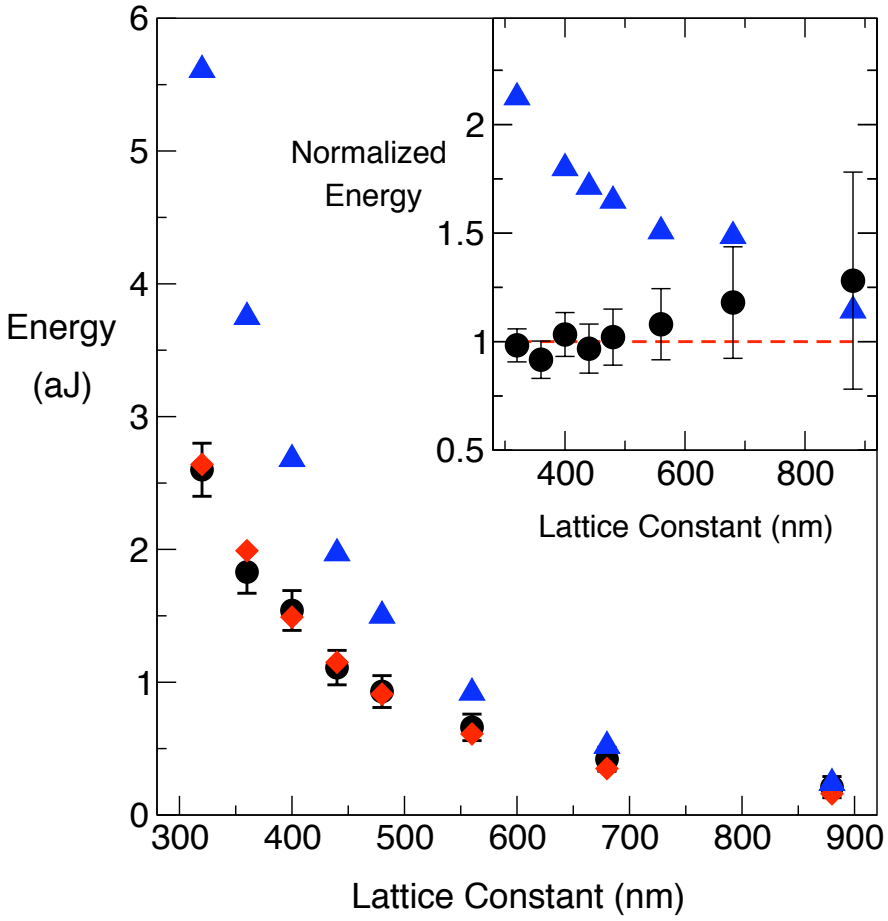

Figure 2.4. The specific vertex energy $\overline{E}$ of demagnetized lattices (dots) compared to the calculated energy of a type-II vertex (E_{II}, diamonds) and the specific energy of a purely random tiling (triangles) for a range of array lattice constants. Error bars incorporate the measured standard deviations of $n_{\mathrm{I}}, n_{\mathrm{II}}, n_{\mathrm{III}}, n_{\mathrm{IV}}$ across multiple arrays, plus a 5% uncertainty in the micromagnetics. The inset shows the specific vertex energy and the random tiling energy, normalized to the pure type-II vertex energy at each lattice constant. One attojoule is 7.25×10^4 Kelvins

This large energy scale suppresses thermal fluctuations, so the spin configurations obtained after demagnetization are static.

2.3.3 The Energy Manifold

If the fractional populations of the four vertex types are denoted $n_{\rm I}$, $n_{\rm II}$, $n_{\rm III}$, $n_{\rm IV}$, then the specific vertex energy is given by

$$\overline{E} = E_{\rm I} n_{\rm I} + E_{\rm II} n_{\rm II} + E_{\rm III} n_{\rm III} + E_{\rm IV} n_{\rm IV}, \tag{2.2}$$

and population fractions can be extracted from magnetic force microscopy on demagnetized arrays.

The measured specific vertex energy, plotted in Figure 2.4, *closely tracks that of a pure type-II tiling*: $\overline{E} \approx E_{\rm II}$. Even samples subjected to an abbreviated anneal protocol, whose residual magnetization is 60% of the saturation value, obey this energetic constraint, as does the original fully polarized sample. This striking relationship does not arise from simple random averaging– the same plot also shows the average vertex energy of a random tiling, wherein each vertex type occurs according to its multiplicity. Apparently, the rotational demagnetization protocol, which begins with an array polarized into a uniform type-II tiling, does not significantly reduce the vertex energy; rather, it moves the configuration about within that energy manifold, reducing the total magnetostatic energy only through a reduction in the long-range demagnetization fields [3]. We take this experimental observation as given, and explore its consequences.

The reason behind the energy ansatz, and whether it arises coincidentally from counteracting kinetic tendencies or coherently from a cooperative process, is still elusive. The dynamical origin of this behavior remains to be explained, and may relate to the step size chosen experimentally being the maximal decrement in absolute field that successfully demagnetizes the array. More recent experimental results on different arrays with demagnetization protocols that include smaller step sizes seems to break the E_{II} manifold. Although as yet we have not characterized these lower energy states, the same maximization procedure described below works well in predicting the vertex populations, although under an energy constraint that is now assumed from the data.

[3] The external field couples most strongly and coherently to the large collective dipole moments associated with any long-ranged demagnetization fields.

2.3.4 Maximum Likelihood of the Outcome of Demagnetization

.

Population fractions for different demagnetized samples at the same lattice constant are very similar, presumably reflecting some well-defined underlying state. Individual islands for samples with lattice constants of 320 and 560 nm show no significant correlations in moment orientation between successive demagnetization runs, so the moments are not pinned by static structural disorder in island shape.

All samples analyzed below had a residual magnetization $M_r \lesssim 10\%$. Only at the largest lattice constants, where the island-island interactions are weakest, does the specific energy approach the random value, i.e. that for equal probabilities for each of the 16 vertices.

During demagnetization, the rotating sample is placed in a time varying magnetic field: at first, the field is large enough to polarize all the islands into a type-II configuration. As the field magnitude drops, it carves defects inside that background. These defects, treated as a non-interacting gas, may appear as types I, II, III or IV, but the background within which they live is purely type-II. The density of defected vertices, ρ, relates the fractional populations of each vertex type within the defected population, written as $\nu_{\rm I}$, $\nu_{\rm II}$, $\nu_{\rm III}$ and $\nu_{\rm IV}$, to the total populations $n_{\rm I}$, $n_{\rm II}$, $n_{\rm III}$, $n_{\rm IV}$ via

$$\begin{aligned} n_{\rm I} &= \rho\nu_{\rm I} \\ n_{\rm III} &= \rho\nu_{\rm III} \\ n_{\rm IV} &= \rho\nu_{\rm IV} \\ n_{\rm II} &= (1-\rho) + \rho\nu_{\rm II}. \end{aligned} \tag{2.3}$$

We adopt a vertex-gas approximation, wherein each vertex is treated as an independent entity. Vertex models of fully degenerate square-ice [61] and water-ice [11] work well, and nearly all the correlations in our experimental data are

contained in the vertices [4]. Thus there are

$$\frac{N!}{(N-D)!\prod_\alpha N_\alpha!} \tag{2.4}$$

ways to tear $D = \rho N$ defects in the N vertices of a polarized tiling, allocated among the four vertex types with distribution $N_\alpha = \rho\nu_\alpha$, $\alpha = \mathrm{I}, \ldots, \mathrm{IV}$.

We model the demagnetization protocol as a one-step non-equilibrium stochastic process at the vertex level. To obtain the most likely outcome of the vertex populations after demagnetization, we maximize the logarithm of the multiplicity,

$$s = -\left[\rho\ln\rho + (1-\rho)\ln(1-\rho)\right] + \rho\sigma, \tag{2.5}$$

formally an entropy, under an energy constraint $\overline{E} = E_{\mathrm{II}}$. The second term of Equation 2.5

$$\begin{aligned}\sigma = \; & - \; \nu_{\mathrm{I}}\ln\left(\frac{\nu_{\mathrm{I}}}{2}\right) - \nu_{\mathrm{II}}\ln\left(\frac{\nu_{\mathrm{II}}}{4}\right) \\ & - \; \nu_{\mathrm{III}}\ln\left(\frac{\nu_{\mathrm{III}}}{8}\right) - \nu_{\mathrm{IV}}\ln\left(\frac{\nu_{\mathrm{IV}}}{2}\right),\end{aligned} \tag{2.6}$$

is the entropy of an ensemble of vertices α, each with probability ν_α and given multiplicity. Maximization of this this entropy for the actual vertex population n_α given by Equations 2.3, or $-n_{\mathrm{I}}\ln\frac{1}{2}n_{\mathrm{I}} - n_{\mathrm{II}}\ln\frac{1}{4}n_{\mathrm{II}} - n_{\mathrm{III}}\ln\frac{1}{8}n_{\mathrm{III}} - n_{\mathrm{IV}}\ln\frac{1}{2}n_{\mathrm{IV}}$ returns populations in only modest agreement with the experimental results for type-II, as seen in Figure 2.5: demagnetization is not thermal equilibration; our system is not ergodic.

Since background vertices all contribute E_{II} to the energy, the energy constraint is relevant only in the maximization of the inner entropy σ: $E_{\mathrm{I}}\nu_{\mathrm{I}} + E_{\mathrm{II}}\nu_{\mathrm{II}} + E_{\mathrm{III}}\nu_{\mathrm{III}} + E_{\mathrm{IV}}\nu_{\mathrm{IV}} = E_{\mathrm{II}}$. The defect population fractions that result are written $\{\nu_\alpha^*\}$. Next, s is maximized relative to the total defect population ρ with σ evaluated at $\{\nu_\alpha^*\}$, yielding $\rho^* = 1/(e^{-\sigma^*}+1)$. The residual magnetization (as a fraction of the saturation magnetization, which is pure type-II) is bounded above by the background

[4]Monte Carlo simulations in naive thermal equilibrium provide more general support for a vertex model. For example, vertex energies corresponding to the 320 nm lattice yields populations within a few percent of the vertex gas predictions for temperatures above about $1.3\,(E_{\mathrm{II}} - E_{\mathrm{I}})$, which is comparable to T_{eff} for that array. However, keep in mind that the state described in the main text is not the naive 16-vertex equilibrium state.

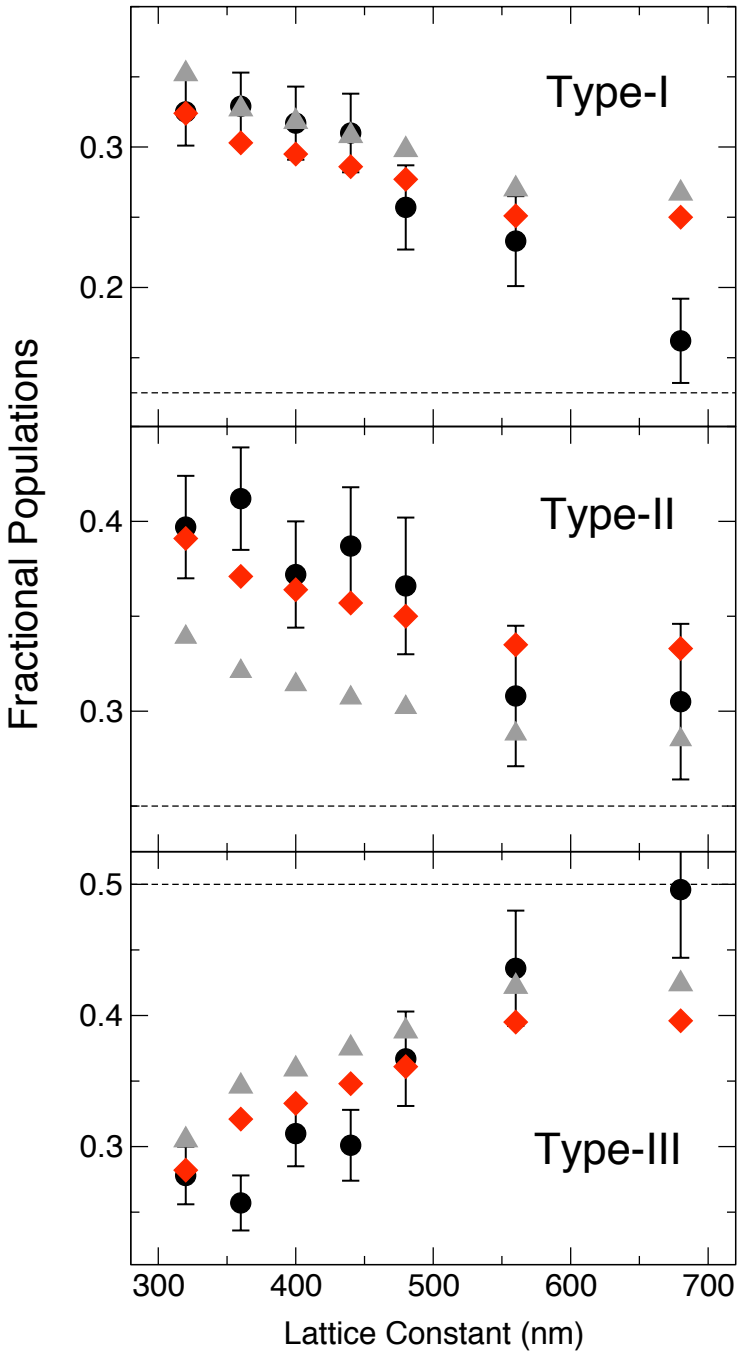

Figure 2.5. Experimental population fractions of vertex types (dots) compared to the values predicted by maximizing the entropy on the type-II vertex energy manifold, with (diamonds) and without (triangles) the background contribution. Dashed lines give the population fraction of a random tiling. Error bars represent statistical counting errors in the populations.

fraction: $M_r \leq 1 - \rho$ ($M_r = N^{-1}\sqrt{(M_1^2 + M_2^2)/2}$ where N is the number of unit cells and $M_1,\ M_2 = \pm 1$ are the magnetic moments of the two islands within a unit cell).

2.3.5 Results and Comparison with Data

The vertex population fractions obtained by this procedure are compared to the experimental results in Figure 2.5. The agreement is good, with no adjustable parameters. This agreement, if taken to verify the model, implies a striking feature in the process of rotational demagnetization: in probabilistic terms, the background state stands on equal footing with each of the defect states. Considering the history of each island's magnet state during demagnetization (in the rotating frame), this suggests that each vertex has a single opportunity to leave the background state and all histories are equally probable. If one introduces an anomalous multiplicity q of the background (where $q = 0$ corresponds to a fully equilibrated background-free scenario) to control the relative likelihood of a vertex remaining in the background, the best fit to the data is obtained when $q \simeq 1$.

As the lattice constant increases, the energy difference between types I and II increases faster than that between II and III. Therefore, under the energy constraint, the ratio $n_{\mathrm{III}}/n_{\mathrm{I}}$ increases: the defected sample acquires larger multiplicity and ρ must increase; hence type-III increase and type-II decrease. The fraction of type-IV is too small to make strong statements, although its population increase at larger lattice constants is also predicted by theory. The predictions are least accurate at large lattice constant, where island-island interactions are weak and the system deviates most strongly from the manifold of constant vertex energy (see inset of Figure 2.4). At the largest lattice constants, the experimental population fractions approach the random-tiling values expected for non-interacting islands. Assuming that the random tiling fraction holds for the defected vertices (i.e. $\nu_{\mathrm{II}} = 0.25$) and using the residual magnetization of the 680 nm sample (10%) as an estimate of $\rho \approx 1 - M_r = 0.9$, one obtains $n_{\mathrm{II}} \approx 0.1 + 0.9 \times 0.25 = 0.32$, close to the experimental value of 0.31. A similar relation works for a 880 nm lattice, not shown.

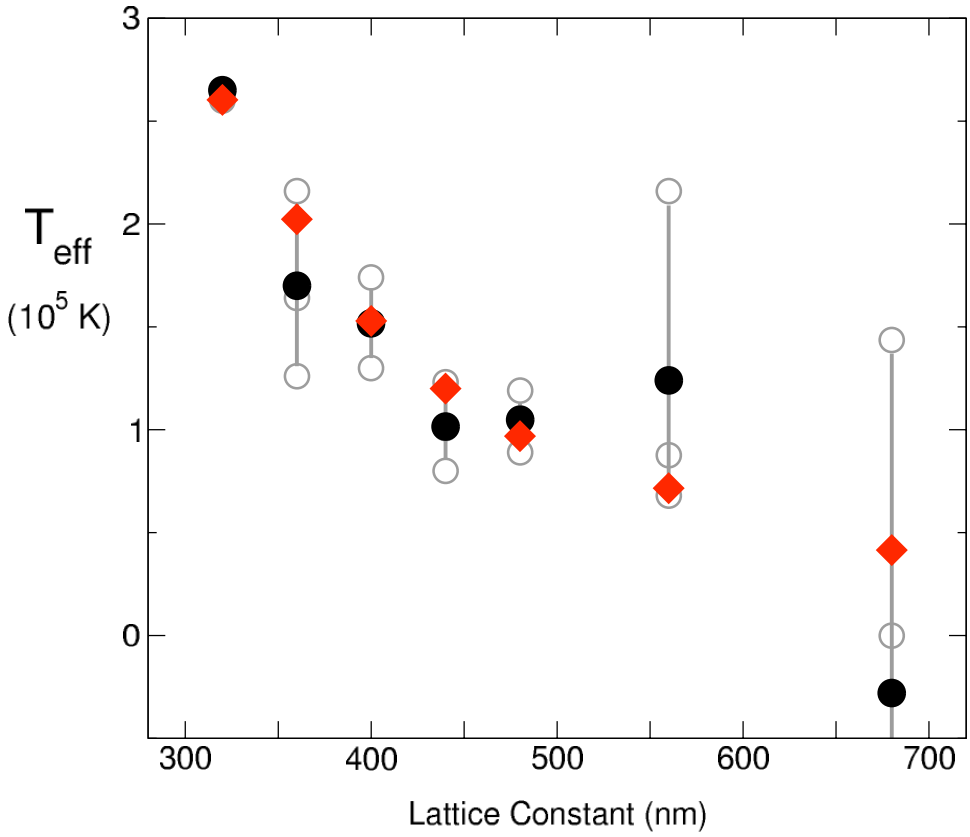

Figure 2.6. Effective temperatures extracted from the three ratios of type I, II, III vertex populations (open circles) and their average (closed circles) compared to the effective temperature of the background/defect model (diamonds). At smaller lattice constants where interactions are most important, the effective temperatures extracted from the vertex populations are consistent with entropy maximization in the background/defect model. At the largest array spacings we enter a random tiling regime.

2.3.6 Effective Temperature

Temperature is a single parameter that contains all available information about a disordered state in thermal equilibrium. However, many disordered systems, such as granular materials or foams, have interaction energy scales greatly exceeding the traditional thermodynamic temperature: describing their disorder is less simple. It remains controversial whether, in what sense, and under what circumstances such a system may possess an effective temperature. One can check if our system has an effective temperature in the traditional sense by setting the ratios of four vertex populations to their putative Boltzmann weights and extracting the result-

ing temperatures. This naive approach does not work: different ratios suggest different temperatures. But with the aid of the background ansatz, a consistent effective temperature can be extracted. The maximization of σ under the vertex energy constraint returns, for the *defected* vertices, relative populations in the form of Boltzmann factors:

$$\frac{\nu_\alpha}{\nu_\lambda} = \frac{q_\alpha}{q_\lambda} e^{-\beta(E_\alpha - E_\lambda)}. \tag{2.7}$$

The indices α, λ represent vertex types and q_α, q_λ their multiplicities. β^{-1} is an effective temperature, set by the entropy maximization. The ratios of the n's, the populations that can be extracted experimentally, are not simply Boltzmann factors. If ρ is taken as known from the entropy maximization, then the ν's can be related to the experimental n's by Equation 2.3. Omitting the relatively rare type-IV vertices (which have a larger statistical uncertainty), the three independent ratios amongst vertex types I, II and III produce a consistent effective temperature in the frustrated regime, as shown in Figure 2.6. The deviations at the largest lattice constants, where the interactions are less important, signal a transition to the random tiling regimen.

2.3.7 Conclusion

In summary, we have shown that a lattice of artificial spin ice, despite the absence of thermal fluctuations, can be described within a thermodynamic framework. A demagnetized state with an extensive residual entropy (similar to that seen in water and spin ice) lives on a sub-manifold of constant vertex energy, equilibrated against a residual background. All nontrivial structure in the microstate can be subsumed into the background component, leaving a Gibbs-like ensemble, with a consistent effective temperature, for the remainder. Thermodynamics, as expressed by entropy maximization, can be defined and the experimental data well described with no adjustable parameters. The reason behind the energy ansatz, and whether it arises coincidentally from counteracting kinetic tendencies or coherently from a cooperative process, is still elusive. A partial explanation can be provided: entropy maximization on the vertex gas under the constraint of a fixed specific vertex energy yields the largest background fraction when $\overline{E}$ is constrained to the specific vertex energy of the background. If the value of the constraint deviates from that

of the background, then the presence of a background demands an ever-larger energetic correction from the defects in order to bring the overall vertex energy in accord with the constraint; this suppresses the entropy of the defect set. If one is to have a constraint, then the value of it that maximizes the overall system entropy is E_{II}.

Chapter 3

More Cylinders: Carbon Nanotubes, a Bi-Continuum Formalism

"It is nice to know that the computer understands the problem. But I would like to understand it, too."

Eugene Wigner

3.1 Limits of Current Models

Vibrations in carbon nanostructures such as nanotubes, fullerenes, or graphene sheets [12, 13, 14] have a ubiquitous influence on transport, electronic, optical, and thermal response. Scattering from optical phonons limits transport of current in otherwise ballistic nanotube conductors [66, 67]. Twist deformations open bandgaps in metallic tubes [68, 69] with many consequences: from shifts of the frequencies of vibrations, to electromechanical effects under doping. Ballistic phonons transport heat in nanotubes with great efficiency [70, 71, 72]. Resonant Raman spectroscopy uses vibration frequencies to unambiguously identify the wrapping indices (n,m) of a tube. At the same time it can record variation in size and length under doping [73, 74, 75, 76]. Electron-phonon interactions may ultimately limit the performance of two-dimensional graphene electron gases [77, 78].

Analytical continuum models of elastic response have been applied to study vibration of carbon nanotubes. Typically borrowed from macroscopic theory of elasticity, either they cannot describe optical modes [79] or introduce ad hoc modification to try to reproduce the richness of the atomic description [80, 81, 82].

Computationally intensive atomistic techniques often lack simplified model descriptions that can facilitate insight, yet continuum analytical models [12, 79, 80, 13] cannot describe optical phonons or the non-linear disperison of acoustic modes at the edge of the Brillouin zone, generally neglect atomistic detail and/or address it by means of ad hoc phenomenological approaches [81, 82], e.g. by connecting the macroscopic strain tensor to a suitable microscopicdescription [84]. Although continuum models are restricted to relatively long-wavelength physics, they *can* describe atomic-scale phenomena, by incorporating a separate continuum field for each sublattice [85]: in graphene, two fields.

To overcome difficulties of previously accepted models in a familiar and easily manageable framework we introduce an analytical "bi-continuum" model that nevertheless represents the full atomistic detail of the graphenic lattice, including optical modes, nonlinear phonon dispersion, electromechanical effects and even the hexagonal graphenic Brillouin zone, a construct generally held to be exclusively atomistic. The deduction of the model will be based only upon consideration of symmetry.

3.2 Review of Elasticity of Continua

For the benefit of the reader we will briefly summarize the fundamentals of elasticity of continuum macroscopic bodies, as it appears in standard publications [86].

The mechanics of solid bodies considered as continua describes their deformations under external stress by assigning a displacement vector field between the undeformed (x_i) and deformed (x'_i) configuration.

$$u^i(x) = x'^i - x^i. \tag{3.1}$$

It is easy to show that the metric tensor changes under deformation so that the

distance between two points $\mathrm{d}l^2 = \mathrm{d}x^i \mathrm{d}x_i$ becomes

$$\mathrm{d}l'^2 = (\delta_{ij} + 2u_{ij})\mathrm{d}x^i \mathrm{d}x^j, \tag{3.2}$$

where, at the first order in the field, u_{ij}, the strain tensor, is the symmetrizaton $u_{ij} = \partial_{(i} u_{j)}$ or

$$u_{ij} = \frac{1}{2}\left(\partial_i u_j + \partial_j u_i\right). \tag{3.3}$$

and describes the local strain of the continuum. One can indeed prove that the deformation can be locally decomposed into a strain and a rotation

$$u_i(x + \mathrm{d}x) - u_i(x) = u_{ij}\mathrm{d}x^j + \epsilon_{ijk}\theta^j \mathrm{d}x^k \tag{3.4}$$

where $\theta_i = \epsilon_{ijk}\partial^j u^k$ is the locally defined angle of rotation.

The density of elastic energy V of the deformation must be invariant under global rotation. Hence at lowest order in u^i (harmonic approximation), it can only contain u^{ij}. Its form can be dictated by the symmetry of the problem. For an isotropic, homogeneous continuum we have

$$V = \mu\, u^{ij} u_{ij} + \frac{\lambda}{2}\, u^i_i u^j_j, \tag{3.5}$$

where μ, λ are called the Lamé symbols.

For a massive continuum, with density ρ, from Lagrangian density

$$L = \frac{1}{2}\rho \dot{u}^2 - V \tag{3.6}$$

one derives the equation of motion

$$\rho \ddot{u}_i = \frac{\partial}{\partial x_j}\frac{\partial V}{\partial u_{ij}}. \tag{3.7}$$

which clearly shows that $\partial_j \frac{\partial V}{\partial u_{ij}}$ is the concentrated force acting on the element of volume, and thus

$$\sigma^{ij} = \frac{\partial V}{\partial u_{ij}} \tag{3.8}$$

is the stress tensor, that describes the action of an internal part of the body on an

adjacent part. For the energy given in Equation 3.5 we have

$$\sigma^{ij} = 2\mu u^{ij} + \lambda \delta^{ij} u^k_k. \tag{3.9}$$

The solution of Equation 3.7 by longitudinal and transverse plane waves $u^i = u^i_o \exp i(k^s x_s - \omega t)$ returns two dispersionless, linear branches of speed of sound

$$\begin{cases} v_L = \sqrt{(2\mu + \lambda)/\rho} \\ v_T = \sqrt{\mu/\rho} \end{cases} . \tag{3.10}$$

While simple and elegant, it is apparent how this formalism is ill-equipped for treatment of non-macroscopic bodies (and many features of macroscopic bodies as well).

As mesoscopic system, graphene and carbon nanotubes share some of the feature of macroscopic bodies, but with an added complexity coming from their atomic structure. The continuum model does not control the full degrees of freedom of the honeycomb lattice, thus cannot account for optical modes, nor can it be used to describe electromechanical effects.

We will now show that by endowing each sublattice of the graphenic honeycomb with an elastic field these difficulties can be overcome.

3.3 The Bi-Continuum Formalism in Graphene

3.3.1 Elastic Energy

The honeycomb lattice of graphene can be decomposed into the two interlaced triangular sub-lattices of Figure 3.1. To take care of all its degrees of freedom, we describe in-plane elastic deformations of the sub-lattices via two 2-D vector fields, $u^i(x)$, $v^i(x)$, $i = 1, 2$, and their strain tensors $u^{ij} = \partial^{(i} u^{j)}$ and $v^{ij} = \partial^{(j} v^{i)}$ [86].

As a functional of u, v, the areal density of elastic energy contains direct and cross terms:

$$V[u, v] = d[u] + d[v] + c[u, v]. \tag{3.11}$$

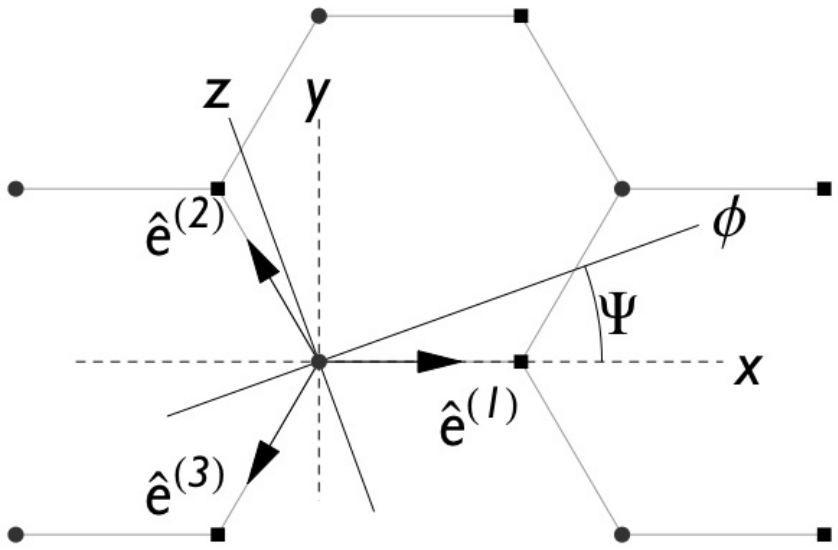

Figure 3.1. The two interlaced sub-lattices (circles and squares) that form the honeycomb structure, and the three unit vectors $\hat{e}^{(l)}$ used in the text. ϕ, z are cylindrical coordinates of the nanotube, while $\Psi = \pi/6 - \theta_c$, with θ_c the chiral angle.

The six-fold symmetry of sub-lattices ensures isotropy of the direct terms [86]:

$$d[u] = \mu'\, u^{ij} u_{ij} + \frac{\lambda'}{2}\, u_i^i u_j^j. \tag{3.12}$$

We will prove at the end of this section that symmetry dictates the form of the cross term

$$\begin{aligned} c[u,v] &= 2\,\mu u^{ij} v_{ij} + \lambda u_i^i v_j^j \\ &+ \alpha\,(u-v)^2 \\ &- \beta\, e_{ijk}\left(u^{ij}+v^{ij}\right)\left(u^k - v^k\right)\ . \end{aligned} \tag{3.13}$$

The tensor e_{ijk} is invariant under the C_{3v} group and can be represented by the three unit vectors $\{\hat{e}^{(l)}\}_{l=1,3}$ of Figure 3.1,

$$e_{ijk} = \frac{4}{3}\sum_{l=1}^{3} \hat{e}_i^{(l)} \hat{e}_j^{(l)} \hat{e}_k^{(l)}. \tag{3.14}$$

Only the last term of the cross contribution to energy, Equation 3.14, is not invari-

ant under general rotation. In carbon nanotubes, it depends on the helical angle θ_c:

$$\begin{cases} e_{\phi,\phi,\phi} = -e_{\phi,z,z} = -\sin(3\theta_c) \\ e_{z,z,z} = -e_{\phi,\phi,z} = -\cos(3\theta_c) \end{cases}, \tag{3.15}$$

where ϕ, z are the cylindrical coordinates as in Figure 3.1. ($\theta_c = 30^o$ deg for an (n,n) tube).

This elastic energy density, the lowest-order approximation in both derivatives and fields, contains six parameters, which we normalize to the sub-lattice surface density σ_s, so that the elastic energy is

$$W = \int \sigma_s V \, d^2x. \tag{3.16}$$

The parameters μ' and λ', being confined to one sublattice, describe next-neighbor interactions; the cross terms μ and λ describe nearest-neighbor interaction; α describes the stiffness against relative shifts of the sublattices; β determines the strength of the rotational symmetry breaking and so contains all information about the point group symmetry of graphene.

The out-of-plane displacements, $u_\perp(x)$, $v_\perp(x)$, do not couple with the in-plane u^i, v^i in the harmonic limit: invariance under simultaneous sign change of $u_\perp$ and $v_\perp$ prevents it, for flat sheets. Introducing $2p(x) = u(x) + v(x)$ and $2q(x) = u(x) - v(x)$, $V_\perp$ must be invariant under $p_\perp \to p_\perp + L(x)$, where $L(x)$ is a linear function in the plane: $V_\perp$ can contain only second (and higher) derivatives in $p_\perp$. Again, symmetry dictates

$$\begin{aligned} V_\perp &= 4\alpha_\perp q_\perp^2 - 4\,\alpha'_\perp \partial_i q_\perp \partial^i q_\perp + 4\beta_\perp e_{ijk}\,\partial^k q_\perp \partial^{ij} p_\perp \\ &+ 2\mu^+_\perp \partial_{ij} p_\perp \partial^{ij} p_\perp + \lambda^+_\perp \partial^i_i p_\perp \partial^i_i p_\perp \\ &- 2\mu^-_\perp \partial_{ij} q_\perp \partial^{ij} q_\perp - \lambda^-_\perp \partial^i_i q_\perp \partial^i_i q_\perp. \end{aligned} \tag{3.17}$$

Equation 3.17 predicts that the frequency of the $k = 0$ out-of-plane optical mode is $\omega_\perp = 2\sqrt{\alpha_\perp}$, and that the out-of-plane acoustic branch is quadratic at small wave-vector, as expected.

We now prove Equation 3.13 on the basis of considerations of symmetry. The term $c[u, v]$ must be invariant under the combination of $2\pi/6$ rotations and the

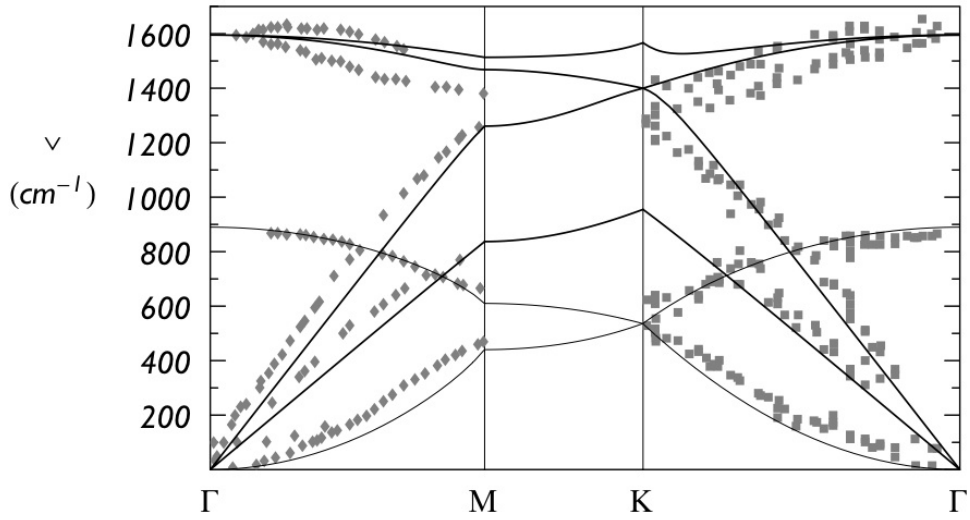

Figure 3.2. Bi-continuum phonons compared to EELS data (diamonds [87] and squares [88]), fitting to the entire Brillouin zone.

exchange of fields $u \leftrightarrow v$. This symmetry, plus reflection through the x axis (Figure 3.1), imply C_{3v} invariance. There is also a field translation invariance: $u(x) \to u(x)+p$, $v(x) \to v(x)+p$. The objects u^i, v^j, u^{ij}, and v^{ij} can be combined pairwise only into tensors of rank two, three and four; thus $c[u,v]$ decomposes into three parts.

The first part has terms like $u^i v^j$; symmetry then implies the form $\alpha(u-v)^2$ with $\alpha > 0$ to ensure an energy minimum.

The second part has terms like $u^{ij}v^{kl}$; the only admissible form is $2\mu u^{ij}v_{ij} + \lambda u^i_i v^j_j$.

The third part contains only rank three terms such as $u^{ij}v^k$ contracted with a C_{3v} invariant tensor e_{ijk}, giving $e_{ijk}u^{ij}v^k$. By requiring invariance under $2\pi/6$ rotations conjugated with sub-lattice switching, and also the field translation invariance, we obtain the form $e_{ijk}u^{ij}(u^k - v^k) + e^*_{ijk}v^{ij}(v^k - u^k)$, where the star means a $2\pi/6$ rotation. Since C_{3v} invariance implies $e^*_{ijk} = -e_{ijk}$ we finally obtain the third row of equation (3.13).

3.3.2 Equations of Motion, Vibrations

Taking

$$\kappa = \frac{1}{2}\sigma_s \left(\dot{u}^2 + \dot{v}^2\right) \tag{3.18}$$

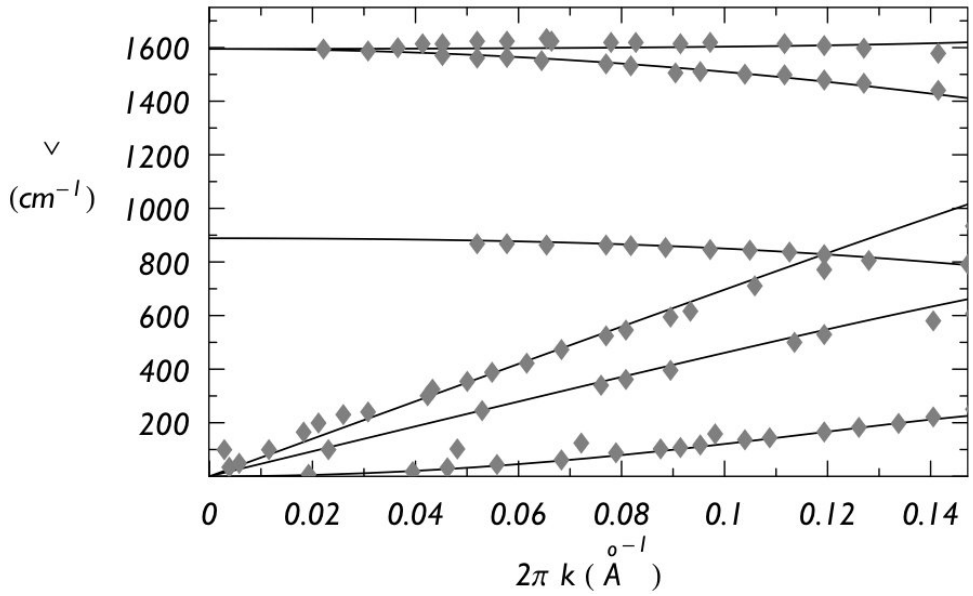

Figure 3.3. Bi-continuum phonons compared to EELS data (diamonds) [87], fitting around Γ along $\Gamma \rightarrow M$.

as the surface density of kinetic energy, the equations of motion can be deduced:

$$\begin{cases} \ddot{u}^i = \partial_j \sigma^{ij}_{(u)} - 2\alpha\,(u^i - v^i) + \beta\, e_{lm}{}^i \left(v^{lm} + u^{lm}\right) \\ \ddot{v}^i = \partial_j \sigma^{ij}_{(v)} + 2\alpha\,(u^i - v^i) - \beta\, e_{lm}{}^i \left(v^{lm} + u^{lm}\right) \end{cases} \tag{3.19}$$

where σ^{ij}_u, σ^{ij}_v are the sub-lattice 2-D stress tensors. In terms of u, v:

$$\begin{cases} \sigma^{ij}_{(u)} & = 2\mu'\, u^{ij} + \lambda'\, \delta^{ij} u^k_k + 2\mu\, v^{ij} + \lambda\, \delta^{ij} v^k_k \\ & \quad -\beta\, e^{ij}{}_k \left(u^k - v^k\right) \\ \sigma^{ij}_{(v)} & = 2\mu'\, v^{ij} + \lambda'\, \delta^{ij} v^k_k + 2\mu\, u^{ij} + \lambda\, \delta^{ij} u^k_k \\ & \quad -\beta\, e^{ij}{}_k \left(u^k - v^k\right) \end{cases} \tag{3.20}$$

As expected, α determines the frequency of two degenerate $k = 0$ optical modes: ${\omega_\Gamma}^2 = 4\,\alpha$.

The bi-continuum phonons are much more richly structured than in a traditional continuum model: they include all the optical branches, show nonlinear dispersion at large wavevector, and even display the main features of the Brillouin zone, all without sacrificing the advantages of a continuum framework. Plane-wave solutions of Equations 3.19 returns an analytically solvable fourth-order secular

Parameters	Γ	BZ
v_L	21 Km s^{-1}	16.5 Km s^{-1}
v_T	14 Km s^{-1}	10.8 Km s^{-1}
$(-2\mu + 2\mu' - \lambda + \lambda' + \beta^2/\alpha)$	$\left(4.4 \text{ Km s}^{-1}\right)^2$	$-\left(8.7 \text{ Km s}^{-1}\right)^2$
$(\mu - \mu')^{1/2}$	15.6 Km s^{-1}	6.6 Km s^{-1}
$\ell \equiv \beta/\alpha$	0.3 Å.	0.24 Å

Table 3.1. Parameters from the fit around Γ along $\Gamma \to M$, and to the Brillouin Zone (Figures 3.2, 3.3).

equation in $\omega(k)$, yielding two acoustic and two optical branches. The longitudinal branches cross at the vertices of a hexagon. Since the two-field elastic energy density respects the point group symmetry of the graphene lattice, this hexagon is oriented just as the graphene Brillouin zone; elastic parameters can be constrained so that the crossing point coincides with the K point of graphene. A similar argument holds for the out-of-plane modes: strikingly, one can construct the correct Brillouin zone within a continuum model.

Figure 3.2 compares the bi-continuum phonons to electron-energy-loss spectroscopy (EELS) data [87, 88] for parameters fitted to the full Brillouin zone; figure 3.3 for parameters fitted just around Γ. Table 3.1 reports these parameters. An extension to higher derivatives would improve the agreement.

3.3.3 Uniform Deformations

For uniform deformations, the usual macroscopic elastic energy of graphene, which is the same of the homogeneous and isotropic of Equation 3.6, with its Lamé coefficients can be obtained from V in the following way.

Equations 3.19 shows that static, uniform solutions must have identical deformations on both lattices: $u^{ij} = v^{ij}$. We considering the inner displacement $2q^i \equiv u^i - v^i$ and obtain, from Equations 3.19,

$$2q^i = \ell \, e_{lm}{}^i u^{lm} = \ell \, e_{lm}{}^i v^{lm}, \tag{3.21}$$

where

$$\ell = \beta/\alpha \tag{3.22}$$

is a characteristic length of the system that describes the strength of the coupling between the inner displacement and the strain. From Equation 3.21 we have that anisotropic ($2\gamma = u^{xx} - u^{yy}$) and shear ($\eta = u^{xy}$) strains produce internal displacements $q^x = \ell\,\gamma$ and $q^y = -\ell\,\eta$ (Figure 3.4) respectively.

Since $u^{i,j} = v^{ij}$, under uniform deformations (or in the approximation of long wavelengths) the elastic energy can be simplified to $W_u = \int V_u \sigma_g \, d^2x$ where $\sigma_g = 2\sigma_s = 2.26$ g cm^{-2} is the surface density of graphene, V_u is given by

$$\begin{aligned} V_u[u,q] &= \left(\mu_R + \frac{\beta^2}{\alpha}\right) u^{ij}u_{ij} + \frac{1}{2}\left(\lambda_R - \frac{\beta^2}{\alpha}\right) u^i_i u^j_j \\ &+ 2\alpha\, q^2 - 2\,\beta\, e_{ijk} u^{ij} q^k. \end{aligned} \tag{3.23}$$

To show that

$$\begin{cases} \mu_R \equiv \mu + \mu' - \frac{\beta^2}{\alpha} \\ \lambda_R \equiv \lambda + \lambda' + \frac{\beta^2}{\alpha} \end{cases} \tag{3.24}$$

are the measurable Lamé coefficients of graphene [86] we can regain regain the expression of the macroscopic elastic energy of graphene. We notice that macroscopic problems do not distinguish between the two sublatices; by eliminating q^i in Equation 3.23 through Equations 3.14 and 3.21 we obtain the familiar, isotropic,

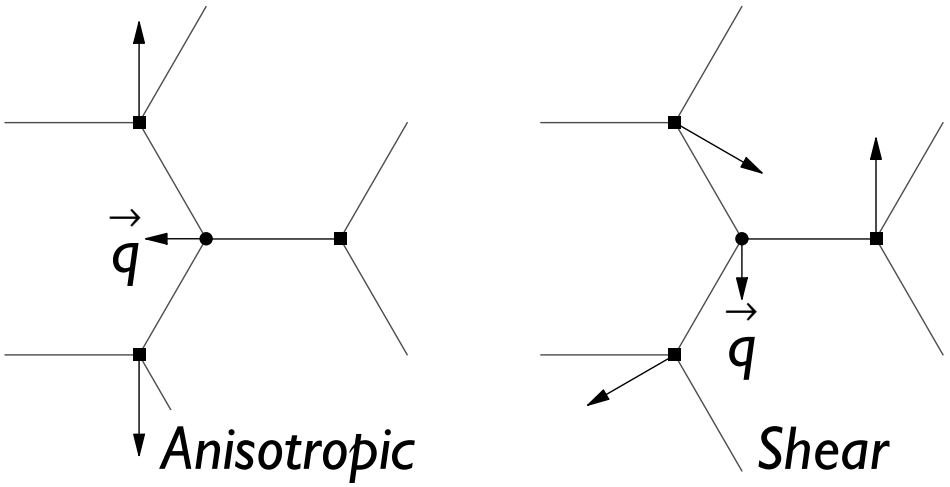

Figure 3.4. Bottom: anisotropic ($u^{xx} = u^{xy} = 0$, $u^{yy} = 2\,\gamma$, $q^x = \ell\,\gamma$), shear ($u^{xx} = u^{yy} = 0$, $u^{xy} = \eta$, $q^y = -\ell\,\eta$) strain.

macroscopic energy for graphene, as promised

$$V_u = \mu_R u^{ij} u_{ij} + \frac{\lambda}{2}_R u^i_i u^j_j. \tag{3.25}$$

Correctly, in the long wavelength limit Equations 3.19 returns the familiar (cfr. Equations 3.10) longitudinal and transverse speeds of sound in terms of the Lamé coefficients: $v_L^2 = 2\mu_R + \lambda_R$, $v_T^2 = \mu_R$.

3.4 The Bi-Continuum Formalism in Carbon Nanotubes

The bi-continuum model provides a unified framework for nanotube mechanics which can describe all current computational results on the coupling of nanotube phonons to each other (e.g. breathing-to-Raman modes or longitudinal-to-transverse modes in helical tubes), to static structural distortions and to the nanotube electronic structure .

In the cylindrical geometry, with coordinates $\{r, \phi, z\}$, a coupling between the tangential displacements u^i, and the radial $u^r = u_\perp$ appears in V (Equation 3.11) via

$$u^{\phi\phi} = \left(\partial_\phi u^\phi + u^r\right)/r \tag{3.26}$$

(and similarly for v), which accounts for the emergence of new optical modes, as the Radial Breathing Mode.

Generally speaking, the chiral vector of the carbon nanotube breaks the hexagonal symmetry and allows for new terms to be introduced in V as curvature corrections, which for simplicity we will not consider here. These terms can be found easily by contracting the vector z^i to tensors respective of the honeycomb lattice symmetry, constructed with u, v as shown before. An example will be provided by the second line of Equation 3.45. Also, even with the present functional form for V, it is clear that all the parameters will depend upon r through an expansion in terms of a^2/r^2. Different problems will suggest different leading corrections.

3.4.1 Vibrations

We will now consider uniform solutions ($u = u_o e^{-i\omega t}$, $v = v_o e^{-i\omega t}$) of the equations of motion. One finds that any dependence on the tube's helicity can be subsumed into new axes $\{\xi, \zeta\}$ that are rotated by an angle $3\theta_c$ with respect to the base of the nanotube:

$$\begin{cases} \xi = \phi \cos 3\theta_c + z \sin 3\theta_c \\ \zeta = -\phi \sin 3\theta_c + z \cos 3\theta_c \end{cases} . \tag{3.27}$$

In terms of $p = (u+v)/2$, $q = (u-v)/2$ we obtain $p^\xi, p^\zeta = 0$ and

$$\begin{cases} q^\zeta \left(\omega^2 - 4\alpha\right) + 2\frac{\beta}{r} p^r = 0 \\ p^r \left(\omega^2 - \frac{v_L^2 + \beta^2/\alpha}{r^2}\right) + 2\frac{\beta}{r} q^\zeta = 0 \\ q^\xi \left(\omega^2 - 4\alpha\right) = 0 \\ q^r \left(\omega^2 - 4\alpha_\perp + \frac{2\mu - 2\mu' + \lambda - \lambda'}{r^2}\right) = 0 \end{cases} . \tag{3.28}$$

Unlike traditional continuum models which cannot describe optical modes, or standard atomistic descriptions which cannot be solved analytically, the two-field continuum model enables an exact analytical solution for a coupling between the radial breathing mode and the graphite-like optical mode through the first two of Equations in 3.28); radial breathing mode induces a shear in the sub-lattices, $u^{\phi\phi} = v^{\phi\phi} = u^r/r$, which couples with the internal displacement through β, and vice versa. Thus, the radial breathing mode is not purely radial, but has a longitudinal component

$$q_B^z = \frac{\ell}{2r} \cos 3\theta_c \tag{3.29}$$

The functional dependence on the angle shown in Equation 3.29 was seen in a force constant numerical calculation [89].

Expansion in powers of l/r of the radial breathing mode frequency reveals the coupling as a correction to the one-field continuum result of Mahan, v_L/r [79]:

$$\omega_B = \frac{v_L}{r} \left[1 - \frac{1}{8} \left(\frac{\ell}{r}\right)^2 + O\left(\frac{\ell}{r}\right)^4 \right] . \tag{3.30}$$

The graphite-like optical modes of chiral tubes are $\omega_\xi = \sqrt{4\,\alpha}$, $\omega_\zeta/\omega_\xi = 1 + \frac{1}{8}\left(\frac{l}{r}\right)^2 + O\left(\frac{l}{r}\right)^4$. They are also of mixed longitudinal/transverse character except

for armchair and zig-zag nanotubes. Instead the out of plane optical mode

$$\omega_\perp = \left(4\alpha_\perp - \frac{2\mu - 2\mu' + \lambda - \lambda'}{r^2}\right)^{1/2} \tag{3.31}$$

is purely radial.

Kürti *et al.* have reported different DFT values with (ω_B) and without ($\tilde{\omega}_B$) coupling with graphite-like optical modes [90]. Using their data with our theory predictions ($r^2\left(\tilde{\omega}_B^2 - \omega_B^2\right) \to \beta^2/\alpha$ as $r \to \infty$) we obtain strengths of the coupling $\ell \equiv \beta/\alpha = 0.25$ Å for non metallic zig-zag and 0.27 Å for armchairs, in good agreement with our values (0.24 Å and 0.30 Å) from the fit of graphene phonons.

The acoustic modes contain the same longitudinal and transverse speeds of sound of the standard continuum [79]

$$\begin{cases} c_T = v_T \\ c_L^2 = 4v_T^2(1 - v_T^2/v_L^2) \end{cases} . \tag{3.32}$$

for transverse (twist) and longitudinal modes; their eigenvectors deviates slightly from purely transverse and longitudinal. While the average displacement p is longitudinal/transverse, the internal $q = (u-v)/2$ points along the ξ axis for transverse modes , and the ζ axis for the longitudinal. The actual trajectories of atoms are thus ellipses squeezed along the longitudinal or transverse direction. They reduce to purely transverse(longitudinal) only in the case of zig-zag (armchair) nanotubes.

The internal displacement after a stretch or a twist of a nanotube can be calculated from Eq 3.23: q^i makes an angle $3\theta_c - \pi/2$ (stretch), or $3\theta_c$ (twist) with the base of the cylinder (the ϕ axes in Figure 3.1). The absolute value of q is $l\frac{r\Delta\phi}{L}$ for stretch and $q = l(1+\nu)\frac{\Delta L}{L}$ for twist, with $\nu = 1 - 2v_T^2/v_L^2$ the Poisson ratio.

3.5 Electromechanical Effects

3.5.1 Incorporating Tight Binding in the Bi-Continuum

The two-field formalism takes into account the full degrees of freedom of the atomistic structure of graphene, and can thus be joined to a description of its band structure to describe electron-lattice coupling to both acoustic and optical modes.

We will proceed by incorporating a tight-binding model [13]. In this framework energy bands are obtained as Lagrange multipliers when minimizing the hamiltonian in the class of localized wave-functions of the form

$$\phi_I(x) = \sum_R e^{ik\cdot R}\psi_I(x+R) \tag{3.33}$$

where ψ_I is the atomic wave-fucntion for the $I = A, B$ atom in the lattice and the sum runs over the unit cells. One finds [13] for the valence and conduction band of graphene at the next nearest neighbors, and neglecting $\langle\psi_A|\psi_B\rangle$

$$\epsilon = H_{AA} \pm |H_{AB}| \tag{3.34}$$

where

$$H_{AA} = \epsilon_{2p} + \sum_{l=1}^{3} t_1^{(l)} \cos\left(k\cdot a^{(l)}\right) \tag{3.35}$$

and

$$|H_{AB}|^2 = \epsilon_c(k)^2 - \epsilon_v(k)^2 = \sum_l t^{(l)} + 2\sum_{m>l} t^{(l)}t^{(m)} \cos\left(k\cdot a^{(n)}\right), \tag{3.36}$$

where $a^{(n)} \equiv e^{(l)} - e^{(m)}$, and $n(l,m)$ is cyclic in $\{1,2,3\}$ (e.g. $a^{(3)} \equiv e^{(1)} - e^{(2)}$), $e_{2p} = \langle\psi_A(x)|H|\psi_A(x)\rangle$, $t_1^{(l)} = \langle\psi_A(x)|H|\psi_A(x+a^{(l)})\rangle$ the next nearest neighbor hopping integral, $t^{(l)} = \langle\psi_A(x)|H|\psi_B(x)\rangle$ the nearest neighbor hopping integral.

The hopping integrals $t^{(l)}$, $t_1^{(l)}$ have negative values. We assume they depend only on distance, and thus $\mathrm{d}|t| = -\tau\mathrm{d}|e|/e$, $\mathrm{d}|t_1| = -\tau_1\mathrm{d}|a|/a$, where e is the interatomic distance, and τ, τ_1 unknown positive parameters. Now, since for instance (cfr. Figure 3.1)

$$\mathrm{d}|e^{(l)}| = \hat{e}^{(l),i}\mathrm{d}e_i^{(l)} = \hat{e}_i^{(l)}\left(v^i(x+e^{(l)}) - u^i(x)\right) = \hat{e}_i^{(l)}\left(v^{ij}e_i^{(l)} - q^i\right) \tag{3.37}$$

and considering that for uniform deformations $u^{ij} = v^{ij} = p^{ij}$ we obtain that the nearest neighbors hopping integrals are modulated by the in-plane elastic deformations:

$$\mathrm{d}|t^{(l)}| = -\tau\,\hat{e}_i^{(l)}\hat{e}_j^{(l)}u^{ij} + \tau\,\hat{e}_i^{(l)}q^i/e. \tag{3.38}$$

Similarly for the next nearest neighbors hopping integrals

$$\mathrm{d}|t_1^{(l)}| = -\tau_1 \, \hat{a}_i^{(l)} \hat{a}_j^{(l)} v^{ij}. \tag{3.39}$$

These last two equations incorporates tight binding into the bi-continuum formalism.

3.5.2 Doping Induced Deformations

The bi-continuum model enable us to access several phenomena absent in simplified models that only take into accunt the length of the tube [83]. Doping-induced structural deformations can be studied by minimizing the total energy (elastic plus doped electrons)

$$E_T = W_u + \Delta E_e \tag{3.40}$$

where W_u is given by Equation 3.23.

According to Equations 3.35, 3.36, two effects are involved in the doping induced deformations: the variation of the position of the fermi energy, and the change in bandgap. Let's consider a zig-zag nanotube of indices (n,0). We expand

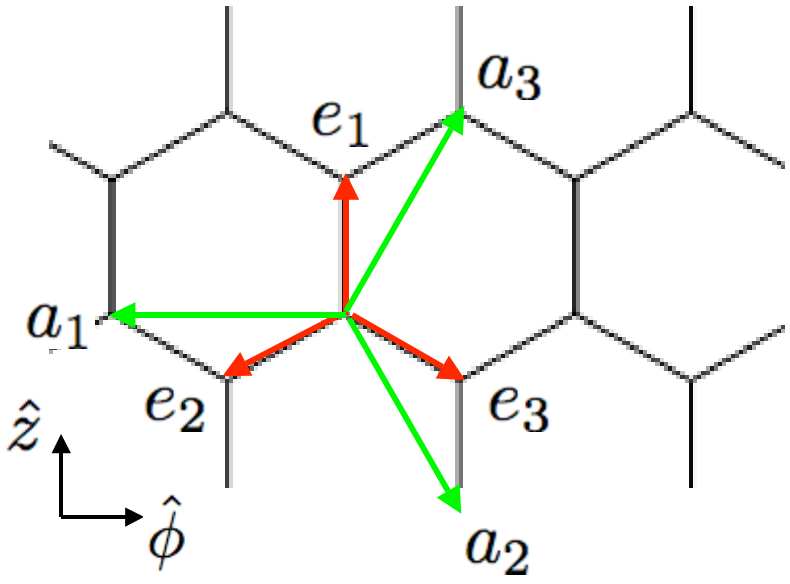

Figure 3.5. Vectors $e^{(l)}$, $a^{(l)}$, and unit vectors $\hat{z}$, $\hat{\phi}$ for a zig-zag nanotube.

Equations 3.35, 3.36 around the K point of the Brillouin zone, or $k = K + \eta$, using

$$\cos\left(k \cdot a^{(l)}\right) = -\frac{1}{2} - \frac{\sqrt{3}}{2}\eta \cdot a^{(l)} + \frac{1}{4}\left(\eta \cdot a^{(l)}\right)^2 . \tag{3.41}$$

The band structure of carbon nanotubes can be deduced from that of graphene by *zone folding* [13]: in summary the Brillouin zone of graphene is "sliced" in discrete segments corresponding to the angular quantization of the wave-functions. From Figure 3.1 we find the angular quantization condition $k \cdot \hat{\phi}\ r = j$, with j integer; consequently, for non metallic zig-zag tubes ($n \mod 3 \neq 0$) the valence and conduction bands lie on a segment in the Brillouin zone of graphene, parallel to the axis of the nanotube at a distance $1/3r$ from the K point, and located on the right or left if $n \mod 3$ is 1 or 2 respectively, as in Figure 3.6.

From Equations 3.33-3.41, using $\eta = \hat{z}k_z \pm \hat{\phi}/3r$ (+ for $n \mod 3 = 1$, − for $n \mod 3 = 2$) the valence and conductance band under deformation can be obtained. By finding the lowest point of the conduction band one concludes that the extra

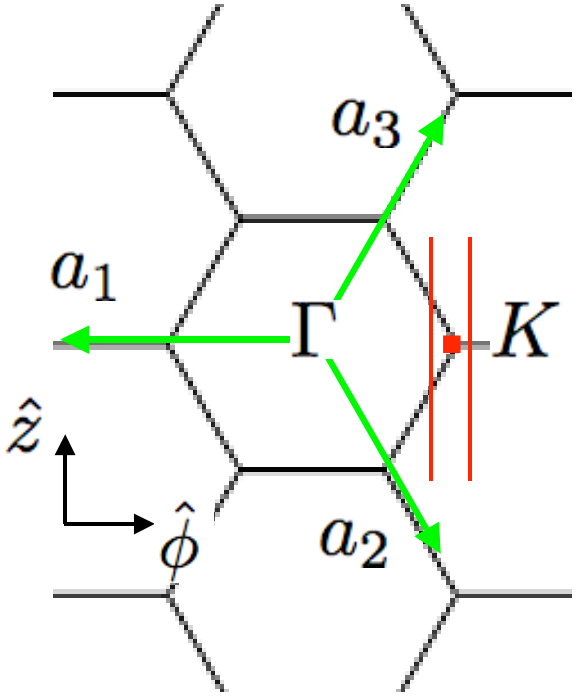

Figure 3.6. Brillouin zone for a zig-zag nanotube: the valence and conduction bands lay on a segment (in red in teh figure) in the Brillouin zone of graphene, parallel to the axis of the nanotube at a distance $1/3r$ from the K point (red square), and located on the right or left if $n \mod 3$ is 1 or 2 respectively

energy brought by doping is, at first order in the fields, in the number of dopant electrons per atom ρ_e, and in a/r:

$$\frac{\Delta E_e}{N_C} = \frac{\rho_e}{4}\left[\pm\tau\left(u^{xx} - u^{yy} - 2\frac{q^x}{e}\right) + 3\tau_1\left(u^{xx} + u^{yy}\right)\right], \tag{3.42}$$

N_C being the number of carbon atoms.

The minimization of the total energy E_T of Equation 3.40 returns a linear systems in the fields which is non homogeneous for $\rho_e \neq 0$. We find the following changes in the axial bond-length ($\mathrm{d}b_{ax} = eu^{zz} - q^z$):

$$\mathrm{d}b_{ax} = \pm\frac{\rho_e\tau}{2m_C\omega_{opt}^2 e} \tag{3.43}$$

where m_C is the mass of the carbon atom. The sign is positive (negative) for $n \mod 3 = 2$ ($n \mod 3 = 1$). Recent DFT results of Margine *et al.* [94] show shrinking or stretching of b_{ax} for $(n = 16, 13)$ or $(n = 14, 11)$ tubes respectively, as predicted by Equation 3.43.

The shrinking of the axial bond determines an up-shift in the longitudinal graphite-like optical mode and might explain recent Raman results that point toward anomalous bond contraction under doping in semiconducting nanotubes [91, 92].

They found positive lengthening in the second case ($n = 14, 11$). For the cases with $n \mod 3 = 2$ the lenghtening they found was less than in the case $n \mod 3 = 1$. As for us, we find the change in length ($\mathrm{d}L/L = u^{zz}$)

$$\mathrm{d}L/L = \frac{\rho_e\tau}{8m_C v_T^2}\left[\pm\left(1 - \frac{\ell}{e}\right) + \frac{3\tau_1}{2\tau}\frac{2\mu_R + \lambda_R}{\mu_R + \lambda_R}\right]. \tag{3.44}$$

Equation 3.44 shows indeed a lower slope - perhaps even a negative one if $\tau_1 < 0.3\tau$ using our parameters - for the lengthening of $n \mod 3 = 2$ zig-zag nanotubes.

3.5.3 Band-Gap Opening, Phonon Softening in Carbon Nanotubes

Lattice deformations open gaps in metallic tubes, and these gaps in turn affect vibrational frequencies. To find the band gap we minimized the expression in Equation 3.36 under general deformation on the "sliced"' segment of Brillouin zone which is closer to the K point. This time we do it for the general metallic nanotube.

From Equations 3.38, 3.36 we find the band gap opened by strain in a metallic nanotube to be

$$\begin{aligned} \frac{\Delta^2}{(3\tau)^2} &= \frac{1}{2}u^{ij}u_{ij} - \frac{1}{4}u^i_i u^i_i - \frac{1}{e}\,e_{ijk}u^{ij}q^k \\ &+ \frac{1}{e^2}\left(\hat{z}_i q^i\right)^2 + \frac{1}{e}\,e_{ijk}\hat{\phi}^k u^{ij}\hat{\phi}_h q^h - \frac{1}{4}\left(e_{ijk}u^{ij}\hat{\phi}^k\right)^2. \end{aligned} \tag{3.45}$$

In the second line of equation (3.45) the symmetry of the honeycomb lattice is broken by the unit vectors $\hat{\phi}^i, \hat{z}^i$. In terms of $2\gamma' \equiv u^{\phi\phi} - u^{zz}$, $\eta' \equiv u^{\phi z}$, q^z, we obtain for the band-gap

$$\Delta = 3\tau\left|q^z/e + \gamma'\cos(3\theta_c) + \eta'\sin(3\theta_c)\right|. \tag{3.46}$$

This latter result corrects and extends a well known previous equation, found by Yang within a one-field continuum model [69], that neglected the inner displacement (i.e. $q^i = 0$). In some situations the coupling to the inner displacement is essential, such as the self trapping of electrons to a local deformation that lowers the bandgap of a semi-metallic nanotube.

Opening bandgaps in metallic nanotubes causes several shifts in observed quantities. The term proportional to q_z^2 in Equation (3.45) show that longitudinal optical modes open a bandgap in metallic tubes of any helicity; the elastic energy lowers by a term proportional to the square of the bandgap, leading to a the softening of longitudinal optical frequency in metallic nanotubes, as revealed by a recent DFT study [93]. Eqn. (3.45) predicts also a softening of the radial breathing mode

in metallic nanotubes

$$\frac{\delta\omega_B}{\omega_B} = -A\cos^2(3\theta_c) \tag{3.47}$$

and relates it to the optical softening, with $A = (1-\ell/e)\omega_{opt}\delta\omega_{opt}e^2/4v_L^2$, ω_{opt} the graphite-like optical mode, and $\delta\omega_{opt}$ its softening in metallic tubes . We predict the highest softening for zig-zag tubes as seen in DFT [90]. We estimate $A \simeq 2\%$. Many other shifts can be predicted in going from non metallic to metallic nanotubes: e.g., the speed of sound for the twist mode softens by

$$\frac{\Delta c_t}{c_t} = -\frac{v_L^2}{2v_T^2}A\sin^2(3\theta_c)\,, \tag{3.48}$$

or $\simeq 2.2\%$ in armchair tubes.

3.6 Conclusion

In summary, a symmetrized two-field continuum model of graphene and carbon nanotubes can access many physical effects for which the naïve continuum model fails, such as nonlinear phonon dispersion, zone-edge degeneracies, coupling to optical modes and electromechanical effects. A full range of vibrational-electronic-elastic couplings, which were absent from previous continuum models or happened upon in an ad hoc fashion in computational work, can now be understood within a unified analytical framework.

Extending the formalism to include higher-order effects arising from curvature or metallic character (i.e. symmetry breaking terms containing $\hat{\phi}^i$, $\hat{z}^i$, as in Equation 3.45), anharmonicity (terms higher order in u^{ij}, v^{ij}), or long-distance interactions (higher partial derivatives) is straightforward.

An extension of the elastic energy to the Boron Nitride nanotube is straightforward (now with different coefficients for each sublattices in the direct terms of Equation 3.12) and might prove useful to study its piezoelectricity.

Bibliography

[1] J. J. Thomson, Philos. Mag. **7**, 237 (1904).

[2] A. R. Bausch, M. J. Bowick, A. Cacciuto, A. D. Dinsmore, M. F. Hsu, D. R. Nelson, M. G. Nikolaides, A. Travesset and D. A. Weitz, Science **299**, 1716 (2003).

[3] A. W. Thompson, *On Growth and Form,* Cambridge Univ. Press, NY, 1959 (first edition 1917)

[4] R. V. Jean, *Phyllotaxis: a Systemic Study in Plant Morphogenesis,* Cambridge Univ. Press, Cambridge 1994.

[5] http://maven.smith.edu/∼phyllo/ provides an overview.

[6] A. H. Church *On the Relation of Phyllotaxis to Mechanical Laws.* (Williams and Norgate, London, 1904)

[7] I. Adler, D. Barabe and R. V. Jean, Ann. Bot. London **80**, 231 (1997).

[8] S. L. Levitov, Phys. Rev. Lett. **66**, 224 (1991)

[9] W. F. Giaque, M. F. Ashley Phys. Rev. **43** 81(1933).

[10] E. M. Schulson JOM **51** 21 (1999).

[11] L. C. Pauling, J. Am. Chem. Soc. **57** 2680 (1935).

[12] S. Iijima, Nature (London) **354**, 56 (1991)

[13] R. Saito, G. Dresselhaus and M. S. Dresselhaus, *Physical properties of Carbon Nanotubes* (Imperial College Press, London 1998).

[14] M. S. Dresselhaus, G. Dresselhaus, and P. C. Eklund, *Science of Fullerences and Carbon Nanotubes* (Academic, New York, 1996).

[15] N. Grew, *The anatomy of plants* (Johnson Reprint Corp., New York, 1965).

[16] E. MacCurdy *The notebooks of Leonardo da Vinci* (Braziller, New York, 1955).

[17] C. Bonnet *Recherches sur l'usage des feuilles dans les plantes* (E. Luzac, fils, Göttingen and Leiden, 1754).

[18] L. E. Sigler *Fibonacci's Liber Abaci* (Springer-Verlag, New York, 2002)

[19] R. V. Jean, B. Denis Multidisciplinarity: a key to phyllotaxis in *Symmetry in Plants* 619-653 (World Scientific, 1998).

[20] L. Bravais, A. Bravais Essai sur la disposition des feuilles curvisé rieés. Annales des Sciences Naturelles Botanique **7** 42-110 193-221; 291-348 **8** 11-42 (1837).

[21] I. Adler Journal of Theoretical Biology **45** 1-79 (1974).

[22] R. V. Jean, D. Barabe Ann. Bot. **88** 173-186 (2001)

[23] A. Frey-Wyssling Nature **173** 596 (1954).

[24] S. F. Albdurnur, K. A. Laki J. Theor. Biol. **104** 599-603 (1983)

[25] R. O. Erickson Science **181** 705-716 (1973).

[26] S. Douady, Y. Couder Phys. Rev. Lett. **68** 2098-2101 (1992).

[27] N. Rivier, R. Occelli, J. Pantaloni and A. Lissowski, J. Phys. **45**, 49 (1984).

[28] L. Chaorong, Z. Xiaona, C. Zexian Triangular and Fibonacci Number Patterns Driven by Stress on Core/Shell Microstructures Science **309** 909-911 (2005)

[29] A. Rahman and J. P. Schiffer Phys. Rev. Lett. **57** 1133-1136 (1986).

[30] T. Shatz, U. Schramm, D. Habs, Nature **412**, 717 (2001)

[31] U. Schramm, T. Shatz, D. Habs, Phys. Rev. E **66**, 036501 (2002).

[32] T. Shätz, U. Schramm and D. Habs Crystalline Ion Beams Nature **412** 717 (2001).

[33] L. S. Levitov EuroPhys. Lett. **14** 533 (1991).

[34] H. W. Lee, L. S. Levitov Universality in Phyllotaxis: a Mechanical Theory in *Symmetry in Plants* 619-653 (World Scientific, 1998).

[35] H. Airy Proc. R. Soc. **21** 176 (1873).

[36] D. M. Deaven and K. M. Ho Phys. Rev. Lett. **75** 288-291 (1995).

[37] J. R. Morris, D. M. Deaven and K. M. Ho Phys. Rev. B **53** R1740-R1743 (1996).

[38] P. D. Shipman and A. C. Newell, Phys. Rev. Lett. **92**, 168102 (2004).

[39] C. Li, X. Zhang, Z. Cao, Science **209**, 909 (2005).

[40] J. Farey, London, Edinburgh and Dublin Phil. Mag. **47**, 385 (1816).

[41] J. H. Conway, and R. K. Guy, *The Book of Numbers* (Springer-Verlag, New York, 1996).

[42] T. Nagell, *Introduction to Number Theory* (Wiley, New York, 1951).

[43] R. Donnelly, Phys. World **10**, 25 (1997).

[44] R. P. Feynman and M. Cohen, Phys. Rev. **102**, 1189 (1956).

[45] F. D. Tappert and N. J. Zabusky, Phys. Rev. Lett. **27**, 1774 (1971).

[46] Z. Y .Li, K. M. Hock and R. E. Palmer Phys. Rev. Lett. **67**, 1562 (1991)

[47] R. D. Diehl, R. McGrath Surf. Sci. Rep. **23** 43 (1996).

[48] D. J. Pochan, Z. Chen, H. Cui, K. Hales, K. Qi, K. L. Wooley, Science **306**, 94 (2004) and references therein.

[49] J. Stambaugh, D. P. Lathrop, E. Ott and W. Losert, Phys. Rev. E **68**, 026207 (2003).

[50] B. Tanatar and D. M. Ceperley, Phys. Rev. B **39**, 5005 (1989).

[51] R. Chitra, T. Gianmarchi and P. Le Doussal, Phys. Rev. B. **65**, 035312 (2001).

[52] M. Remoissenet *Waves Called Solitons* (Springer-Verlag, Berlin, 1999)

[53] A. C. Scott Am. J. Phys. **37**, 52 (1969)

[54] K. Nakajima T. Yamashita, Y. Onodera Phys. Rev. B **45** 3141 (1974)

[55] A. V. Ustinov Physica D **123** 315 (1998)

[56] H. Kleinert *Path Integrals* (World Scientific, Singapore, 1995)

[57] A. Actor Rev. Mod. Phys. **51** 461 (1979)

[58] N. Manton, P. Sutcliffe *Topological Solitons* (Cambridge, 2004)

[59] R. Baxter, *Exactly Solved Models in Statistical Physics* (Academic, New York, 1982).

[60] E. H. Lieb and F. W. Wu, in *Phase Transitions and Critical Phenomena*, vol. 1, C. Domb and M. S. Green, Eds. (Academic, London, 1971).

[61] E. H. Lieb, Phys. Rev. Lett. **18**, 692 (1967).

[62] A. P. Ramirez, A. Hayashi, R. J. Cava, R. Siddharthan, and B. S. Shastry, Nature **399**, 333-335 (1999).

[63] S. T. Bramwell, M. J. P. Gingras Science **294** 5546 (2001)

[64] R. Wang, C. Nisoli, R.S. Freitas, J. Li, W. McConville, B.J. Cooley, M. S. Lund, N. Samarth, C. Leighton, V. H. Crespi and P. Schiffer Nature (London) **439**, 303-306 (2006)

[65] C. E. Shannon and W. Weaver, *The Mathematical Theory of Communication* (Univ. Illinois Press, Urbana IL, 1949).

[66] S. J. Tans, M. H. Devoret, H. Dai, A. Thess, R. E. Smalley, L. J. Geerligs, C. Dekker Nature **386** 474 (1997).

[67] C. L. Kane, E. J. Mele, R. S. Lee, J. E. Fischer, P. Petit, H. Dai, A. Thess, R. E. Smalley, A. R. M. Verschueren, S. J. Tans, and C. Dekker, Europhys. Lett. **41** 683 (1998).

[68] A. Rochefort, P. Avouris, F. Lesage, D. R. Salahub Phys. Rev. B **60** 13824 (1999).

[69] L. Yang and J. Han, Phys. Rev. Lett. **85**, 154 (2000)

[70] S. Berber, Y-K. Kwon, and D. Tománek, Phys. Rev. Lett. **84** 4613 (2000).

[71] H.-Y. Chiu, V. V. Deshpande, H. W. Ch. Postma C. N. Lau, C. Mikó L. Forró, and M. Bockrath Phys. Rev. B **95** 226101 (2005).

[72] P. Kim L. Shi A. Majumdar and P. L. McEuen Phys. Rev. Lett. **87** 215502 (2001).

[73] E. Ritcher, K. R. Subbaswamy Phys. Rev. Lett. **79** 2738 (1997).

[74] R. Saito, A. Jorio, J. H. Hafner, C. M. Lieber, M. Hunter, T. McClure, G. Dresselhaus, and M. S. Dresselhaus Phys. Rev. B **64** 085312 (2001).

[75] A. Jorio, R. Saito, J. H. Hafner, C. M. Lieber, M. Hunter, T. McClure, G. Dresselhaus, and M. S. Dresselhaus, Phys. Rev. Lett. **86** 1118 (2001).

[76] A. Jorio, R. Saito, G. Dresselhaus and M. S. Dresselhaus Phil. Trans. R. Soc. Lond. A **362**, 2311 (2004).

[77] K. S. Novoselov, A. K. Geim, S. V. Morozov, D. Jiang, M. I. Katsnelson, I. V. Grigorieva, S. V. Dubonos and A. A. Firsov. Nature **438** 197 (2005).

[78] S. Y. Zhou, G.-H. Gweon, J. Graf, A. V. Fedorov, C. D. Spataru, R. D. Diehl, Y. Kopelevich, D.-H. Lee, S. G. Louie and A. Lanzara Nature Phys. **2** 595 (2006).

[79] G. D. Mahan, Phys. Rev. B **65**, 235402 (2002).

[80] H. Suzuura and T . Ando, Phys. Rev. B **65**, 235412 (2002). A. Raichura *et al.*, J. Appl. Phys. **94**, 4060 (2003).

[81] F. Comas *et al.*, Phys. Rev. B **47**, 7602 (1993).

[82] L. Chico and R. Prez-lvarez Phys. Rev. B **69**, 35419 (2004).

[83] M. Verissimo-Alves, Belita Koiller, H. Chacham, and R. B. Capaz, Phys. Rev. B **67**, 161401 (2003).

[84] Y. N . Gartstein *et al.*, Phys. Rev. B **68**, 115415 (2003)

[85] R. D. Mindlin in "Mechanics of Generalized Continua, Proceedings of the IUTAM Symposium", 312-320, Springer-Verlag New York (1968)

[86] L. D. Landau, E. M. Lifshitz "Theory of Elasticity" Pergamon Press Oxford (1986).

[87] C. Oshima, T. Aizawa, R. Souda, Y. Ishizawa, and Y. Sumiyoshi, Solid State Commun. **65**, 1601 (1988).

[88] S. Siebentritt, R. Pues, K. H. Rieder, and A. M. Shikin, Phys. Rev. B **55**, 7927 (1997).

[89] E. Dobardžić *et al.*, Phys. Rev. B **68**, 045408 (2003).

[90] J. Kürti *et al.*, New J. Phys.**5**, 125 (2003)

[91] G. Chen, C. A. Furtado, U. J. Kim, and P. C. Eklund Phys. Rev. B **71** 045408 (2005).

[92] G. Chen, C. A. Furtado, S. Bandow, S. Iijima and P. C. Eklund Phys. Rev. B **72** 155406 (2005).

[93] O. Dubay *et al.*, Phys. Rev. Lett. **88**, 235506 (2002).

[94] R. E. Margine *et al.* Submitted to PRL.

Vita

Cristiano Nisoli

Academic

- Maturità, Liceo Classico (Classical School in Humanities) Thesis "The Birth of Tragedy: Three Ways to Read Nietzsche in the XX Century" Grade 60/60
- Laurea in Fisica, Università degli Studi di Milano (Degree in Physics) Thesis "Quantum Oscillations on a Schwarzschild's Background with Cosmological Constant" Grade 110/110
- Ph. D. in Physics, Penn State University, Thesis "Leaves and Stems, Rotons and Solitons, Magnets and Arrays, One Ground State Lost, Many Found, and Two Fields"

Awards

- 2005-2006 Duncan Fellowship
- 2006 15th U.S. National Congress on Theoretical and Applied Mechanics: Travel Award
- 2000 Braddock Fellowship